

Improving Multimodal Learning with Dispersive and Anchoring Regularization

Zixuan Xia^{*1,2} Hao Wang^{*1,2} Pengcheng Weng^{*1,2} Yanyu Qian^{3,2} Yangxin Xu² William Dan^{1,2} Fei Wang²

Abstract

Multimodal learning aims to integrate complementary information from heterogeneous modalities, yet strong optimization alone does not guarantee well-structured representations. Even under carefully balanced training schemes, multimodal models often exhibit geometric pathologies, including intra-modal representation collapse and sample-level cross-modal inconsistency, which degrade both unimodal robustness and multimodal fusion.

We identify representation geometry as a missing control axis in multimodal learning and propose DAGR, a lightweight geometry-aware regularization framework. DAGR enforces two complementary constraints on intermediate embeddings: an intra-modal dispersive regularization that promotes representation diversity, and an inter-modal anchoring regularization that bounds sample-level cross-modal drift without rigid alignment. The proposed regularizer is plug-and-play, requires no architectural modifications, and is compatible with various training paradigms.

Extensive experiments across multiple multimodal benchmarks demonstrate consistent improvements in both multimodal and unimodal performance, showing that explicitly regulating representation geometry effectively mitigates modality trade-offs.

1. Introduction

Multimodal learning aims to integrate complementary information from heterogeneous modalities such as audio, vision, and language (Baltrušaitis et al., 2018). A central challenge in this setting is *modality trade-off*: improving

¹Department of Informatics, University of Bern, Bern, Switzerland ²School of Software Engineering, Xi’an Jiaotong University, Xi’an, China ³College of Computing and Data Science, Nanyang Technological University, Singapore. Correspondence to: Fei Wang <feynmanw@xjtu.edu.cn>.

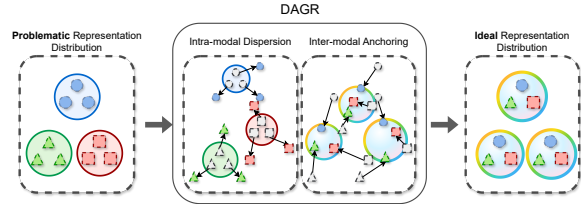


Figure 1. **Geometric pathologies and regularization in multimodal representation learning.** (Left) *Modality-dominated geometry*: embeddings are primarily organized by modality, producing compact modality-specific clusters with weak cross-modal semantic correspondence. (Middle) *Dispersion and anchoring*: intra-modal dispersion prevents low-rank collapse within each modality, while inter-modal anchoring limits excessive sample-level cross-modal drift without enforcing rigid alignment. (Right) *More semantically aligned geometry*: paired samples across modalities become better aligned while retaining modality-specific variation, yielding a more coherent multimodal representation space.

multimodal fusion can come at the cost of weaker unimodal representations, which in turn hurts robustness under missing or corrupted modalities (Wei & Hu, 2024; Chaudhuri et al., 2025). Existing approaches often attribute this phenomenon primarily to optimization issues, such as gradient suppression or objective conflicts across modalities (Wei et al., 2025; Yu et al., 2020). While these factors are important, they do not directly control the geometry of the learned representation space.

In this work, we focus on a complementary perspective: **representation geometry**. Across multimodal training pipelines, we observe two recurring geometric failure modes. The first is **intra-modal collapse**, where embeddings within a modality concentrate in a narrow subspace with reduced diversity and effective dimension. The second is **sample-level cross-modal drift**, where modality-specific embeddings of the same sample become insufficiently aligned in the shared representation space. Together, these pathologies weaken both modality-specific expressiveness and cross-modal cooperation and can contribute to modality trade-offs in downstream fusion. Figure 1 illustrates this progression from geometry dominated by modality to a more semantically aligned representation space.

To mitigate these failure modes, we propose **DAGR** (**D**ispersive and **A**nchoring **G**eometric **R**egularizer), a geometry-aware regularizer for multimodal learning. DAGR

operates along two complementary axes. **(i) Intra-modal dispersion** encourages embeddings within each modality to spread out in the mini-batch, reducing collapse and preserving representation diversity. **(ii) Inter-modal anchoring** constrains excessive sample-level cross-modal drift by upper-bounding the distance between paired embeddings across modalities. Importantly, this anchoring term is a *bounded-drift* constraint rather than a rigid alignment objective: once paired embeddings are sufficiently close, the anchoring gradient vanishes, allowing modality-specific variation to be retained. Because DAGR is applied to intermediate embeddings, it can be incorporated into existing multimodal training pipelines without modifying the underlying architecture.

We evaluated DAGR on supervised multimodal benchmarks including CREMA-D, Kinetics-Sounds, CUBICC and XRF55. In these evaluated settings, DAGR improves multimodal performance and often strengthens unimodal representations as well. Our analysis further shows that these gains co-occur with measurable geometric changes, including reduced cross-modal drift and improved representation diversity. Overall, our contributions are three-fold:

- We identify **intra-modal collapse** and **sample-level cross-modal drift** as two geometric failure modes that contribute to modality trade-offs in multimodal learning.
- We propose DAGR, a dispersion-and-anchor regularizer that improves multimodal representation geometry without architectural changes.
- We provide empirical and theoretical evidence that regulating representation geometry can improve multimodal fusion while often preserving or strengthening unimodal robustness in the evaluated settings.

2. Related Work

2.1. Gradient Optimization for Multimodal Learning

A central challenge in multimodal learning is the *modality trade-off*, where training tends to favor a dominant modality while weakening others. A major line of work addresses this issue from the perspective of *gradient optimization*, including logit or gradient balancing strategies (Zong et al., 2024; Kwon et al., 2025), multi-objective optimization formulations for mitigating gradient conflicts (Sener & Koltun, 2018; Yu et al., 2020; Fernando et al., 2025; Jiang et al., 2025), and decoupled or disentangled training schemes that separate unimodal and fusion supervision (Wang et al., 2024b; Wei et al., 2025). These methods improve multimodal optimization by controlling how training signals are balanced, routed, or projected across modalities. In contrast, our work focuses on a complementary question:

even when optimization is stabilized, the learned representation geometry may still exhibit intra-modal collapse and sample-level cross-modal drift. DAGR therefore complements gradient-centric methods by explicitly regularizing multimodal representation geometry.

2.2. Contrastive Alignment for Balancing Modalities

Another major line of work addresses multimodal learning through *contrastive alignment* objectives, which pull matched cross-modal pairs together and separate mismatched pairs (Radford et al., 2021; Alayrac et al., 2022; Wang & Isola, 2020). These methods improve shared semantic structure across modalities, but recent studies also show that contrastive training can induce modality gaps and other alignment-related geometric effects in the joint space (Yaras et al., 2024; Yi et al., 2025). Related efforts therefore revisit what should be aligned and how alignment should be imposed; for example, CoMM argues that naive alignment can over-emphasize shared factors and proposes a communication-based contrastive objective for richer multimodal interaction (Dufumier et al., 2024). In contrast, DAGR does not enforce stronger global alignment through contrastive discrimination. Instead, it regularizes multimodal geometry by combining intra-modal dispersion with a bounded constraint on sample-level cross-modal drift.

2.3. Geometry-aware Regularization

Recent work increasingly highlights the role of representation geometry in multimodal learning, including dispersion, redundancy reduction, and cross-modal alignment (Wang & Isola, 2020; Zbontar et al., 2021; Bardes et al., 2021). A closely related concurrent direction, in particular, UniAlign (Yin et al., 2026) analyzes two conflicts in multimodal InfoNCE—an alignment–uniformity conflict and an intra-alignment conflict—and proposes to decouple alignment and uniformity for shared-space learning, with a focus on retrieval and generation settings.

Our work is related in spirit but differs in both setting and objective. Rather than revisiting multimodal contrastive learning, we study supervised multimodal classification and fusion, where modality trade-offs can persist even when optimization is stabilized. We focus on two geometric failure modes in this setting: *intra-modal collapse* and *sample-level cross-modal drift*. Correspondingly, DAGR regularizes geometry through two complementary components: intra-modal dispersion to preserve representation diversity, and bounded inter-modal anchoring to limit excessive drift between paired embeddings without enforcing rigid global alignment. As such, DAGR is designed as a plug-and-play regularizer for multimodal fusion pipelines, and is complementary to both gradient-centric balancing methods and alignment-centric shared-space objectives.

3. Methodology

3.1. Problem Setup

We consider supervised multimodal learning with a dataset $\mathcal{D} = \{(x_i, y_i)\}_{i=1}^N$, where each sample $x_i = (x_i^1, \dots, x_i^M)$ consists of M modalities and $y_i \in \{1, \dots, K\}$ is the target label. Each modality x_i^m is mapped by an encoder ϕ_m to an intermediate representation

$$z_i^m = \phi_m(x_i^m) \in \mathbb{R}^d. \quad (1)$$

These representations in modality are then consumed by a downstream multimodal predictor $g(\cdot)$, such as a fusion module followed by a task head, to produce the final prediction.

The standard supervised objective is

$$\mathcal{L}_{\text{task}} = \mathbb{E}_{(x,y) \sim \mathcal{D}} [\ell(g(z^1, \dots, z^M), y)], \quad (2)$$

where $\ell(\cdot, \cdot)$ denotes the task loss. As discussed in Section 1, we focus on two geometric failure modes—*intra-modal collapse* and *sample-level cross-modal drift*—and regularize them at the intermediate representation level.

Our full training objective augments the task loss with the proposed geometric regularizer:

$$\mathcal{L} = \mathcal{L}_{\text{task}} + \lambda_d \mathcal{L}_d + \lambda_a \mathcal{L}_a, \quad (3)$$

where \mathcal{L}_d promotes intra-modal dispersion and \mathcal{L}_a limits excessive cross-modal drift between paired embeddings. **Importantly, DAGR is applied to intermediate embeddings and does not require modifying the underlying multimodal architecture.**

Geometric ambiguity of task supervision. The supervised task loss constrains the predictive content of modality-wise representations, but does not uniquely determine their geometry. In particular, for each modality, there can exist multiple geometrically distinct representations that induce the same logits and hence the same task loss.

Proposition 3.1 (Geometric ambiguity of task-optimal representations). *Consider the decoupled supervised objective $\mathcal{L} = \sum_{m=1}^M \mathcal{L}_{\text{CE}}(W_m z^m, y)$. If $\{z^m\}_{m=1}^M$ is an optimal solution, then there exists a family of modality-wise transformations that preserve the logits, and therefore preserve optimality, while altering the geometry of the representations.*

Proposition 3.1 formalizes that task supervision alone does not exclude geometrically poor solutions, such as collapsed or weakly aligned representations. This motivates introducing an explicit geometric regularizer on intermediate embeddings.

Algorithm 1 Training with DAGR

Require: Encoders $\{\phi_m\}_{m=1}^M$ (params $\{\theta_m\}$); step size η ;
use_pareto, $\beta \in [0, 1]$ or (λ_d, λ_a)

- 1: $\tilde{z}^{(m)} \leftarrow \text{Normalize}(\phi_m(x^{(m)})), \forall m$
- 2: **Compute** \mathcal{L}_d^m and \mathcal{L}_a
- 3: **for** $m = 1$ to M **do**
- 4: $g_{\text{task}}^{(m)} \leftarrow \nabla_{\theta_m} \mathcal{L}_{\text{task}}$
- 5: $g_d^{(m)} \leftarrow \nabla_{\theta_m} \mathcal{L}_d^m$; $g_a^{(m)} \leftarrow \nabla_{\theta_m} \mathcal{L}_a$
- 6: **if** **use_pareto** **then**
- 7: **Solve** α_m^* by Eq. (10)
- 8: $g_{\text{geom}}^{(m)} \leftarrow \beta(\alpha_m^* g_a^{(m)} + (1 - \alpha_m^*) g_d^{(m)})$
- 9: **else**
- 10: $g_{\text{geom}}^{(m)} \leftarrow \lambda_a g_a^{(m)} + \lambda_d g_d^{(m)}$
- 11: **end if**
- 12: $\theta_m \leftarrow \theta_m - \eta(g_{\text{task}}^{(m)} + g_{\text{geom}}^{(m)})$
- 13: **end for**

3.2. DAGR: Dispersive and Anchoring Geometry Regularization

To explicitly regulate multimodal representation geometry, we introduce DAGR (Dispersive and Anchoring Geometry Regularization)—a lightweight and plug-and-play geometric regularizer that complements existing multimodal training pipelines.

Technically, we first apply normalization to the unimodal representations to eliminate scale variations and project features onto a hypersphere. DAGR then enforces two synergistic geometric constraints: (i) a dispersive term that promotes the diversity and discriminability of intra-modal representations, and (ii) an anchoring term that maintains coherent cross-modal consistency. We next introduce the whole procedure in detail.

3.2.1. NORMALIZED UNIMODAL EMBEDDINGS

For each modality $m \in \{1, \dots, M\}$, let $z_i^m \in \mathbb{R}^d$ denote the encoder output for the sample i . Before applying DAGR, we ℓ_2 -normalize each embedding onto the unit hypersphere:

$$\tilde{z}_i^m = \frac{z_i^m}{\|z_i^m\|_2}. \quad (4)$$

This removes scale variation across samples and modalities, so the subsequent regularization acts only on the geometry of the normalized representations. Normalization is used only inside DAGR and does not alter the underlying multimodal architecture.

3.2.2. INTRA-MODAL DISPERSION

To discourage unimodal collapse, DAGR promotes dispersion within each modality on the unit hypersphere. Given a mini-batch \mathcal{B} of size B , we define the intra-modal dispersive

loss as

$$\mathcal{L}_d = \frac{1}{M} \sum_{m=1}^M \mathcal{L}_{\text{disp}}^m, \quad (5)$$

$$\mathcal{L}_{\text{disp}}^m = \log \left(\frac{1}{B(B-1)} \sum_{\substack{i,j \in \mathcal{B} \\ i \neq j}} \exp(-t \|\tilde{z}_i^m - \tilde{z}_j^m\|_2^2) \right), \quad (6)$$

where $t > 0$ controls the interaction scale.

Equation (6) is a uniformity-style radial basis function (RBF) objective applied independently to each modality. It assigns larger penalties to locally crowded configurations, so minimizing it encourages embeddings within the same modality to spread out more uniformly on the unit hypersphere. As a result, the loss improves representation diversity and discourages low-rank collapse in modality-specific features.

We adopt this RBF uniformity form as the default dispersive term throughout the paper. Besides its simplicity, it admits a clean theoretical connection to Rényi-2 entropy and effective-rank control, which we use in Section 3.3. Broader classes of dispersive potentials and their shared repulsive-gradient interpretation are deferred to Appendix A.4.

3.2.3. INTER-MODAL ANCHORING REGULARIZATION

While intra-modal dispersion effectively regularizes uni-modal geometry, it does not explicitly constrain the relative geometric consistency across modalities, which may lead to cross-modal drift in the learned representation space. To mitigate this effect without enforcing full modality invariance, DAGR introduces a *bounded* inter-modal anchoring term that penalizes only *excessive* cross-modal discrepancy beyond a tolerance radius τ . Concretely, we define

$$\mathcal{L}_a = \frac{1}{B} \sum_{i \in \mathcal{B}} \frac{1}{M(M-1)} \sum_{m \neq n} \left(\|\tilde{z}_i^m - \tilde{z}_i^n\|_2 - \tau \right)_+^2, \quad (7)$$

where $(x)_+ = \max(x, 0)$ and \tilde{z}_i^m denotes the ℓ_2 -normalized embedding on the unit hypersphere. Unlike naive alignment objectives that continuously shrink $\|\tilde{z}_i^m - \tilde{z}_i^n\|_2$, the proposed anchoring acts as a soft constraint that *upper-bounds* cross-modal drift up to the tolerance τ , while preserving modality-specific variations within this admissible radius. This bounded-drift behavior is theoretically characterized in Theorem 3.3.

3.2.4. ADAPTIVE PARETO-BALANCED WEIGHTING.

As mentioned in Eq. (3), the final DAGR regularizer is defined as:

$$\mathcal{L}_{\text{DAGR}} = \lambda_d \mathcal{L}_d + \lambda_a \mathcal{L}_a, \quad (8)$$

, which defines DAGR as a weighted sum of \mathcal{L}_d and \mathcal{L}_a , in practice the two terms may induce conflicting gradients on encoder parameters, leading to sensitivity to the choice of (λ_d, λ_a) . To reduce manual tuning, we optionally adopt a Pareto-balanced weighting scheme that dynamically selects the mixing coefficient at each iteration.

Let θ_e denote the encoder parameters and define

$$g_d = \nabla_{\theta_e} \mathcal{L}_d, \quad g_a = \nabla_{\theta_e} \mathcal{L}_a. \quad (9)$$

We seek a convex combination $g(\alpha) = \alpha g_a + (1 - \alpha) g_d$ that yields a stable descent direction by minimizing its norm:

$$\alpha^* = \arg \min_{\alpha \in [0,1]} \|\alpha g_a + (1 - \alpha) g_d\|_2^2. \quad (10)$$

This admits a closed-form solution

$$\alpha^* = \text{clip}_{[0,1]} \left(\frac{\|g_d\|_2^2 - \langle g_a, g_d \rangle}{\|g_a - g_d\|_2^2} \right). \quad (11)$$

We then apply a geometry-gradient injection

$$g_{\text{geom}} = \beta (\alpha^* g_a + (1 - \alpha^*) g_d), \quad (12)$$

where β is a base scaling factor. Equivalently, this corresponds to using iteration-dependent weights $\lambda_a^{(t)} = \beta \alpha^*$ and $\lambda_d^{(t)} = \beta(1 - \alpha^*)$ in Eq. (8). Importantly, we apply Pareto balancing only to encoder parameters θ_e , while keeping the fusion module optimized solely by the task objective, thereby preserving DAGR as a plug-in geometry regularizer without architectural changes.

3.3. Theoretical properties of DAGR

We briefly summarize the two theoretical properties most relevant to our empirical diagnostics. The complete statements, proofs, and auxiliary results are deferred to the Appendix A.

3.3.1. DISPERSION DISCOURAGES LOW-RANK COLLAPSE

For the uniformity-style dispersive loss in Eq. (6), minimizing \mathcal{L}_d encourages higher entropy on the unit hypersphere and therefore discourages low-rank collapse of modality-wise representations.

Theorem 3.2 (Dispersion and effective rank). *Under the uniformity instantiation in Eq. (6), minimizing \mathcal{L}_d is asymptotically related to maximizing the Rényi-2 entropy of the normalized feature distribution. Consequently, stronger dispersion discourages low effective-rank solutions.*

This result motivates our use of effective rank as a geometric diagnostic in Section 4.3.

3.3.2. ANCHORING BOUNDS CROSS-MODAL DRIFT.

Dispersion alone does not resolve the inter-modal inconsistency mode; DAGR addresses this via the anchoring term

\mathcal{L}_a , which couples representations across modalities at the sample level.

Theorem 3.3. Consider the joint objective

$$\mathcal{L}_{\text{total}} = \mathcal{L} + \lambda_a \mathcal{L}_a + \lambda_d \mathcal{L}_d, \quad (13)$$

where $\mathcal{L}_a = \mathbb{E}[(\|\tilde{z}^m - \tilde{z}^n\|_2 - \tau)_+^2]$. Let \tilde{z}_*^m and \tilde{z}_*^n denote optimal representations of two modalities. Then the expected excess cross-modal drift satisfies

$$\mathbb{E}[(\|\tilde{z}_*^m - \tilde{z}_*^n\|_2 - \tau)_+^2] \leq \frac{\delta}{\lambda_a}, \quad (14)$$

where $\delta \geq 0$ captures an irreducible modality gap induced by modality-specific nuisance factors. A formal proof is provided in Appendix A.3.

Remark 3.4. Unlike naive alignment objectives that enforce complete modality invariance, our anchoring formulation does not force $\|z_*^m - z_*^n\| \rightarrow 0$; instead, it suppresses cross-modal drift while allowing modality-specific deviations, which is crucial for preserving complementarity.

4. Experiments

4.1. Datasets and Experimental Setup

We evaluate the proposed method on a diverse set of multimodal benchmarks spanning audio–visual, tri-modal, image–text, and RF-based perception scenarios, including **CREMA-D** (Cao et al., 2014), **Kinetics-Sounds (KS)** (Arandjelovic & Zisserman, 2017), **CUB Image-Captions for Clustering (CUBICC)** (Palumbo et al., 2024) and **XRF55** (Wang et al., 2024a).

For audio–visual benchmarks (CREMA-D and KS), we follow the standardized experimental protocols and data splits provided by DGL (Wei et al., 2025). For image–text clustering on CUBICC, we adopt the official implementation of DCMEM (Gao et al., 2025). Experiments on XRF55 are conducted under the X-Fi framework (Chen & Yang, 2024), which provides unified preprocessing and evaluation for heterogeneous RF and vision modalities, and is also adopted in our concurrent work COMPASS (Wang et al., 2026).

More details about datasets and the training setup are provided in Appendix B.1.

4.2. Main Results on Different Benchmarks

Results on CREMA-D and Kinetics-Sounds. Table 1 summarizes the results on the audio–visual benchmarks CREMA-D and Kinetics-Sounds (KS). All methods are built upon the same DGL backbone, and **DGL + DAGR** corresponds to augmenting DGL with the proposed geometry-aware regularization.

Notably, **DGL + DAGR** improves not only multimodal accuracy but also unimodal performance for both audio and

visual modalities. This behavior contrasts with many multimodal methods that improve fusion accuracy at the expense of unimodal representations, and suggests that explicitly regularizing representation geometry helps preserve modality-specific discriminability while enhancing cross-modal complementarity. Such results demonstrate that geometry-aware regularization effectively mitigates modality trade-offs in audio–visual learning.

Results on CUBICC. We further evaluate the proposed geometry-aware regularization on the CUB Image-Captions for Clustering (CUBICC) benchmark. Table 2 reports clustering results in terms of ACC, NMI, and ARI for image-only, caption-only, and joint representations. Compared to the original DCMEM baseline, augmenting the model with DAGR consistently improves clustering performance across all settings. In particular, for joint representations, our method achieves improvements of +3.5 ACC, +1.3 NMI, and +2.4 ARI, indicating more effective multimodal clustering. Notably, consistent gains are also observed for unimodal representations.

Since clustering performance is highly sensitive to the geometric structure of the embedding space, these results suggest that DAGR effectively reshapes representation geometry by enhancing inter-cluster separability while preserving intra-cluster compactness. Moreover, the consistent improvements on both unimodal and joint representations indicate that DAGR strengthens modality-specific structure without compromising cross-modal alignment, leading to more semantically coherent multimodal embeddings.

Results on XRF55. We further evaluate the proposed method on the XRF55 dataset under the X-Fi benchmark protocol. As shown in Table 3, incorporating DAGR consistently improves recognition accuracy across all modality settings, including unimodal and multimodal combinations.

Overall, across datasets of varying scales and modality compositions, DAGR consistently improves multimodal learning performance without sacrificing unimodal robustness, highlighting its ability to balance cross-modal integration and modality-specific representation quality across a wide range of experimental settings.

4.3. Geometry Diagnostics of DAGR

To validate the geometric effects targeted by DAGR, we analyze the intermediate representation space during training on CREMA-D using three diagnostics: (i) the semantic margin Δ_{sem} , which measures class-wise separability; (ii) the effective rank r_{eff} , which quantifies unimodal representation diversity; and (iii) the cross-modal drift d_{drift} , which measures the average distance between paired cross-modal embeddings. (Detailed explanation of these metrics is provided

Table 1. Main results on CREMA-D and Kinetics-Sounds (KS). We report unimodal and multimodal classification accuracy.

| Method | CREMA-D | | | KS | | |
|--------------------------------|-------------------|-------------------|-------------------|-------------------|-------------------|-------------------|
| | Audio | Visual | Multi | Audio | Visual | Multi |
| G-Blending (Wang et al., 2020) | 58.78 | 58.62 | 69.21 | 46.35 | 51.12 | 69.60 |
| OGM-GE (Peng et al., 2022) | 57.76 | 40.09 | 68.82 | 44.23 | 45.81 | 66.89 |
| PMR(Fan et al., 2023) | 55.11 | 38.34 | 67.44 | 43.61 | 46.67 | 65.70 |
| AGM (Li et al., 2023) | 56.37 | 43.54 | 69.61 | 46.12 | 47.65 | 68.88 |
| MMPareto (Wei & Hu, 2024) | 59.43 | 61.09 | 70.12 | 48.40 | 52.42 | 69.83 |
| D&R (Wei et al., 2024) | 61.11 | 64.57 | 74.32 | 49.78 | 54.88 | 69.10 |
| DGL (Wei et al., 2025) | 62.17±0.79 | 70.31±1.11 | 77.65±1.05 | 50.63±0.54 | 59.83±0.63 | 75.44±0.49 |
| DGL + DAGR (Ours) | 62.98±0.50 | 72.10±0.55 | 78.16±0.38 | 50.83±0.50 | 61.71±0.47 | 77.00±0.44 |
| Imp ↑ | +0.81 | +1.79 | +0.51 | +0.20 | +1.88 | +1.56 |

Table 2. Clustering results on the CUB Image-Captions for Clustering (CUBICC) dataset. We report ACC, NMI, and ARI (%) for image-only, caption-only, and joint representations, and DCMEM +DAGR denotes augmenting DCMEM with the proposed geometry-aware dispersive regularization.

| Method | Image | | | Caption | | | Joint | | |
|-------------------------------|-------------|-------------|-------------|-------------|-------------|-------------|-------------|-------------|-------------|
| | ACC | NMI | ARI | ACC | NMI | ARI | ACC | NMI | ARI |
| MVAE (Wu & Goodman, 2018) | 26.2 | 12.4 | 7.5 | 18.1 | 2.4 | 0.9 | 38.7 | 26.8 | 18.0 |
| MMVAE (Shi et al., 2019) | 23.1 | 12.1 | 6.1 | 14.5 | 1.3 | 0.1 | 15.8 | 1.5 | 0.2 |
| MoPoE (Sutter et al., 2021) | 33.4 | 17.6 | 11.5 | 43.5 | 27.1 | 19.9 | 40.8 | 30.4 | 20.2 |
| MEME (Joy et al., 2021) | 44.8 | 43.4 | 28.4 | 36.3 | 29.5 | 18.6 | 19.8 | 4.8 | 2.1 |
| MMVAE+ (Palumbo et al., 2023) | 27.7 | 11.9 | 7.1 | 48.7 | 36.4 | 26.8 | 64.4 | 52.6 | 44.1 |
| CMVAE (Palumbo et al., 2024) | 67.7 | 58.3 | 47.4 | 65.1 | 53.3 | 42.7 | 73.7 | 67.4 | 57.2 |
| MMVM (Sutter et al., 2024) | 58.9 | 56.9 | 44.5 | 23.9 | 9.4 | 5.4 | 66.8 | 67.0 | 55.5 |
| MVP (Gao & Pu, 2025) | 64.1 | 53.8 | 41.8 | 48.5 | 34.4 | 26.1 | 61.1 | 55.6 | 44.0 |
| DCMEM (Gao et al., 2025) | 87.5 | 79.3 | 73.6 | 72.2 | 56.0 | 48.1 | 86.7 | 78.4 | 72.2 |
| DCMEM + DAGR (Ours) | 89.3 | 79.8 | 76.8 | 74.0 | 56.5 | 48.6 | 90.2 | 79.7 | 74.6 |
| Imp ↑ | +1.8 | +0.5 | +3.2 | +1.8 | +0.5 | +0.5 | +3.5 | +1.3 | +2.4 |

Table 3. Accuracy (%) on the XRF55 dataset under the X-Fi benchmark protocol. **X-Fi** denotes the benchmarked strong baseline in (Chen & Yang, 2024), and **X-Fi + DAGR** augments the corresponding pipeline with the proposed geometry-aware regularization. **Imp↑** reports the absolute improvement over **X-Fi**.

| Modality | X-Fi | X-Fi + DAGR | Imp↑ |
|----------|------------|-------------|--------------|
| R | 82.33±1.23 | 83.57±0.04 | +1.24 |
| W | 64.62±2.33 | 67.36±1.17 | +2.74 |
| RF | 41.60±2.04 | 42.54±0.55 | +0.94 |
| R+W | 89.92±0.74 | 90.74±0.18 | +0.82 |
| R+RF | 83.76±1.70 | 85.84±0.15 | +2.08 |
| W+RF | 67.49±0.36 | 67.95±0.38 | +0.46 |
| R+W+RF | 90.09±0.82 | 91.01±0.06 | +0.92 |

in Appendix C.1) We compare three variants: the **baseline**, **Disp Only** (baseline + intra-modal dispersion only), and DAGR. Together, these diagnostics directly correspond to the two failure modes discussed in Section 1: intra-modal collapse and sample-level cross-modal drift.

Table 4. Geometry diagnostics on CREMA-D. Δ_{sem} measures semantic separability, r_{eff} measures unimodal representation diversity, and d_{drift} measures cross-modal drift between paired embeddings. DAGR improves semantic margin while maintaining strong effective rank and avoiding the drift increase observed in Disp Only.

| Method | $\Delta_{\text{sem}} \uparrow$ | $r_{\text{eff}} \uparrow$ | $d_{\text{drift}} \downarrow$ | Acc. (%)↑ |
|--------------|--|---------------------------|-------------------------------|-------------|
| DGL baseline | 4.5×10^{-4} | 4.09 | 0.505 | 76.6 |
| + Disp Only | 8.5×10^{-4} | 3.99 | 0.718 | 76.0 |
| + DAGR | 7.2×10^{-3} | 4.18 | 0.487 | 76.8 |

Table 4 shows that the DGL baseline suffers from weak semantic separation and non-trivial cross-modal drift. Using the dispersive term alone yields only a marginal gain in Δ_{sem} ($4.5 \times 10^{-4} \rightarrow 8.5 \times 10^{-4}$), but lowers r_{eff} ($4.09 \rightarrow 3.99$) and markedly increases d_{drift} ($0.505 \rightarrow 0.718$), suggesting that dispersion alone does not reliably improve multimodal geometry. By contrast, DAGR substantially improves Δ_{sem} (7.2×10^{-3}), achieves the highest effective rank (4.18), and reduces cross-modal drift to 0.487, which

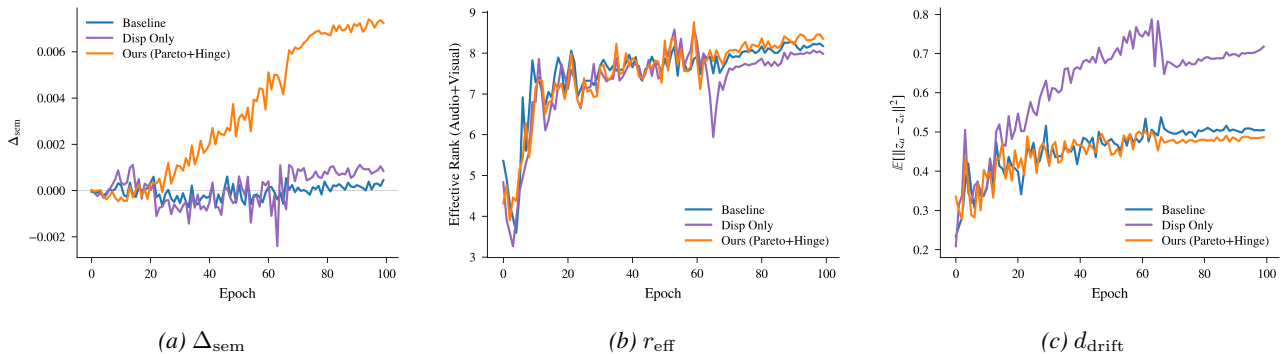


Figure 2. Training-time geometry diagnostics on CREMA-D. **Left:** DAGR steadily increases the semantic margin Δ_{sem} , indicating improved class-wise separation. **Middle:** DAGR maintains strong effective rank, indicating preserved unimodal representation diversity. **Right:** DAGR stabilizes cross-modal drift, whereas `Disp Only` does not control paired cross-modal geometry as effectively. These trends are consistent with the intended roles of DAGR: discouraging collapse and bounding excessive cross-modal drift.

also corresponds to the best classification accuracy (76.8%). This supports the intended role of DAGR: dispersion promotes representation diversity, while anchoring is needed to control excessive cross-modal drift.

Figure 2 further shows how these quantities evolve training. DAGR yields a steady increase in semantic margin, while preserving or slightly improving effective rank relative to the baseline. At the same time, its cross-modal drift remains lower and more stable than that of `Disp Only`, which indicates that dispersion alone is insufficient for controlling paired cross-modal geometry. Overall, these results support the intended mechanism of DAGR: dispersion improves modality-wise representation diversity, and anchoring complements it by limiting excessive sample-level drift across modalities.

4.4. Ablation Studies

Component-wise ablation (dispersion vs. anchoring).

We conduct a component-wise ablation study to disentangle the roles of the two geometric objectives in DAGR: intra-modal dispersion and inter-modal anchoring. Specifically, we evaluate four variants: ① the baseline training pipeline without geometry regularization; ② applying only intra-modal dispersion \mathcal{L}_d ; ③ applying only inter-modal anchoring $\mathcal{L}_{\text{inter}}$; and ④ the full DAGR objective combining both components.

This ablation study provides a quantitative analysis of the complementary roles played by dispersion and anchoring, as summarized in Table 5. When applied individually, each component yields partial improvements. In particular, dispersion alone (②) leads to consistent gains in unimodal accuracy and also improves multimodal performance, suggesting its effectiveness in enhancing intra-modal geometry. Similarly, anchoring alone (③) benefits both unimodal and multimodal settings, with a more pronounced improvement

Table 5. Component-wise ablation of geometry-aware regularization on CREMA-D. We report unimodal (Audio, Visual) and multimodal (Multi) classification accuracy.

| Component | | CREMA-D | | |
|-----------|--------|-------------------|-------------------|-------------------|
| Disp | Anchor | Audio | Visual | Multi |
| | | 62.17±0.79 | 70.31±0.79 | 77.65±0.79 |
| ✓ | | 63.26±0.59 | 71.76±1.00 | 77.81±1.52 |
| | ✓ | 62.55±0.73 | 72.92±0.78 | 77.98±1.11 |
| ✓ | ✓ | 62.98±0.50 | 72.10±0.55 | 78.16±0.38 |

in the multimodal score, indicating its role in stabilizing cross-modal relationships.

Importantly, neither component in isolation achieves uniformly optimal performance across all settings. When dispersion and anchoring are combined (④), the model attains the best overall balance, simultaneously strengthening unimodal robustness and multimodal fusion. This result highlights the complementary nature of the two objectives and underscores the importance of jointly enforcing well-conditioned intra-modal geometry and consistent cross-modal alignment.

Hyper-parameter sensitivity. We further analyze the robustness of DAGR to hyper-parameter choices under two practical usage settings. In the direct regularization formulation, DAGR involves three hyper-parameters, namely λ_d , λ_{inter} , and the temperature τ , which control intra-modal dispersion, inter-modal anchoring, and similarity sharpness, respectively. We sweep these parameters over a wide range on multiple datasets and observe smooth performance trends with well-defined optima, indicating that the method does not rely on fragile tuning.

To improve usability, we additionally adopt a Pareto-based formulation that automatically balances the two geometric

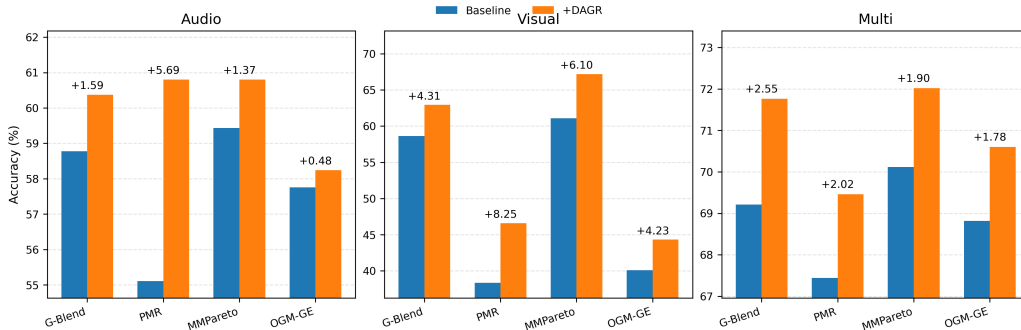


Figure 3. Plug-in generality of DAGR across representative multimodal optimization backbones on CREMA-D.

objectives. Under this setting, only τ and a single trade-off coefficient β need to be tuned, substantially reducing the hyper-parameter search space. Empirically, we find that the Pareto formulation achieves comparable or better performance while exhibiting similar stability in both task metrics (unimodal and multimodal accuracy) and geometry diagnostics (e.g., effective rank and cross-modal drift).

Based on these observations, we use the Pareto-based variant as the default setting in our experiments. See Appendix D.1 for more details.

Robustness to Missing or Corrupted Modalities. In addition to standard ablations, we include a lightweight robustness evaluation to directly assess model behavior under missing or corrupted modalities. Specifically, at test time we progressively drop or corrupt one modality (e.g., random masking or noise injection) and report the degradation curves for both unimodal and multimodal performance, providing a more direct diagnosis of robustness than unimodal accuracy alone, and complements the component-wise ablation by revealing how DAGR affect stability under modality degradation. See Appendix D.2 for more details.

Additional baselines compared with Contrastive Learning. To rule out the possibility that our gains stem from stronger cross-modal coupling or representation normalization, we evaluate several additional baselines on CREMA-D that are closely related to contrastive or invariance-driven objectives. Results are summarized in Appendix D.3.

Plug-in generality. To verify that DAGR is not specific to DGL, we further apply it to four representative multimodal optimization backbones on CREMA-D: G-Blending, PMR, MMPareto, and OGM-GE. As shown in Fig. 3, DAGR yields consistent gains in audio, visual, and multimodal accuracy across all four methods. These results suggest that the geometric regularization induced by DAGR is complementary to diverse multimodal training strategies rather than tied to a particular optimization pipeline.

5. Conclusions, Limitations and Future Work

This work demonstrates that gradient-level optimization alone is insufficient for robust multimodal learning, as representation geometry can remain ill-conditioned even under carefully designed training schemes and carefully tuned objectives. By introducing DAGR, which explicitly promotes intra-modal dispersion and inter-modal anchoring at the geometric level, we consistently improve multimodal performance across audio-visual and heterogeneous multimodal benchmarks. Importantly, these gains are achieved without any other architectural modifications. The proposed method is therefore **plug-and-play**, lightweight, and can be seamlessly integrated into existing state-of-the-art multimodal training pipelines with minimal implementation overhead.

However, our evaluation focuses on medium-scale classification tasks and controlled backbone architectures. Extending this analysis to larger-scale datasets, more diverse task settings (e.g., temporal reasoning, generation, or cross-modal retrieval), and broader model families would further strengthen the empirical understanding of geometry-aware regularization. In particular, studying how geometric constraints interact with large transformer-based multimodal models, attention mechanisms, and temporal structure remains an open and promising direction. More broadly, we believe that similar geometric principles may also benefit self-supervised and weakly supervised multimodal learning, where representation collapse and misalignment are especially pronounced.

Impact Statement

This paper presents work whose goal is to advance the field of multimodal machine learning. There are many potential societal consequences of our work, none of which we feel must be specifically highlighted here.

References

- Alayrac, J.-B., Donahue, J., Luc, P., Miech, A., Barr, I., Hasson, Y., Lenc, K., Mensch, A., Millican, K., Reynolds, M., et al. Flamingo: a visual language model for few-shot learning. *Advances in neural information processing systems*, 35:23716–23736, 2022.
- Arandjelovic, R. and Zisserman, A. Look, listen and learn. In *Proceedings of the IEEE international conference on computer vision*, pp. 609–617, 2017.
- Baltrušaitis, T., Ahuja, C., and Morency, L.-P. Multimodal machine learning: A survey and taxonomy. *IEEE transactions on pattern analysis and machine intelligence*, 41(2):423–443, 2018.
- Bardes, A., Ponce, J., and LeCun, Y. Vicreg: Variance-invariance-covariance regularization for self-supervised learning. *arXiv preprint arXiv:2105.04906*, 2021.
- Cao, H., Cooper, D. G., Keutmann, M. K., Gur, R. C., Nenkova, A., and Verma, R. Crema-d: Crowd-sourced emotional multimodal actors dataset. *IEEE transactions on affective computing*, 5(4):377–390, 2014.
- Chaudhuri, A., Dutta, A., Bui, T., and Georgescu, S. A closer look at multimodal representation collapse. *arXiv preprint arXiv:2505.22483*, 2025.
- Chen, X. and Yang, J. X-fi: A modality-invariant foundation model for multimodal human sensing. *arXiv preprint arXiv:2410.10167*, 2024.
- Dufumier, B., Castillo-Navarro, J., Tuia, D., and Thiran, J.-P. What to align in multimodal contrastive learning? *arXiv preprint arXiv:2409.07402*, 2024.
- Fan, Y., Xu, W., Wang, H., Wang, J., and Guo, S. Pmr: Prototypical modal rebalance for multimodal learning. In *Proceedings of the IEEE/CVF Conference on Computer Vision and Pattern Recognition*, pp. 20029–20038, 2023.
- Fernando, H., Ram, P., Zhou, Y., Dan, S., Samulowitz, H., Baracaldo, N., and Chen, T. Mitigating modality imbalance in multi-modal learning via multi-objective optimization. *arXiv preprint arXiv:2511.06686*, 2025.
- Gao, L., Chen, W., Wang, D., Guo, F., and Liang, C. Disentangled cross-modal representation learning with enhanced mutual supervision. In *The Thirty-ninth Annual Conference on Neural Information Processing Systems*, 2025.
- Gao, X. and Pu, J. Deep incomplete multi-view learning via cyclic permutation of vaes. *arXiv preprint arXiv:2502.11037*, 2025.
- Jiang, Q.-Y., Chi, Z., and Yang, Y. Interactive multimodal learning via flat gradient modification. In *Proceedings of the Thirty-Fourth International Joint Conference on Artificial Intelligence*, pp. 5489–5497, 2025.
- Joy, T., Shi, Y., Torr, P. H., Rainforth, T., Schmon, S. M., and Siddharth, N. Learning multimodal vaes through mutual supervision. *arXiv preprint arXiv:2106.12570*, 2021.
- Kwon, J., Kim, M., Lee, E., Choi, J., and Kim, Y. See-saw modality balance: See gradient, and sew impaired vision-language balance to mitigate dominant modality bias. *arXiv preprint arXiv:2503.13834*, 2025.
- Li, H., Li, X., Hu, P., Lei, Y., Li, C., and Zhou, Y. Boosting multi-modal model performance with adaptive gradient modulation. In *Proceedings of the IEEE/CVF International Conference on Computer Vision*, pp. 22214–22224, 2023.
- Palumbo, E., Daunhawer, I., and Vogt, J. E. Mmvae+: Enhancing the generative quality of multimodal vaes without compromises. In *The Eleventh International Conference on Learning Representations*. OpenReview, 2023.
- Palumbo, E., Manduchi, L., Laguna, S., Chopard, D., and Vogt, J. E. Deep generative clustering with multimodal diffusion variational autoencoders. In *The Twelfth International Conference on Learning Representations*, 2024.
- Peng, X., Wei, Y., Deng, A., Wang, D., and Hu, D. Balanced multimodal learning via on-the-fly gradient modulation. In *Proceedings of the IEEE/CVF conference on computer vision and pattern recognition*, pp. 8238–8247, 2022.
- Radford, A., Kim, J. W., Hallacy, C., Ramesh, A., Goh, G., Agarwal, S., Sastry, G., Askell, A., Mishkin, P., Clark, J., et al. Learning transferable visual models from natural language supervision. In *International conference on machine learning*, pp. 8748–8763. PmLR, 2021.
- Sener, O. and Koltun, V. Multi-task learning as multi-objective optimization. *Advances in neural information processing systems*, 31, 2018.
- Shi, Y., Paige, B., Torr, P., et al. Variational mixture-of-experts autoencoders for multi-modal deep generative models. *Advances in neural information processing systems*, 32, 2019.
- Sutter, T., Meng, Y., Agostini, A., Chopard, D., Fortin, N., Vogt, J., Shahbaba, B., and Mandt, S. Unity by diversity: Improved representation learning for multimodal vaes. *Advances in Neural Information Processing Systems*, 37: 74262–74297, 2024.

- Sutter, T. M., Daunhawer, I., and Vogt, J. E. Generalized multimodal elbo. *arXiv preprint arXiv:2105.02470*, 2021.
- Wang, F., Lv, Y., Zhu, M., Ding, H., and Han, J. Xrf55: A radio frequency dataset for human indoor action analysis. *Proceedings of the ACM on Interactive, Mobile, Wearable and Ubiquitous Technologies*, 8(1):1–34, 2024a.
- Wang, H., Luo, S., Hu, G., and Zhang, J. Gradient-guided modality decoupling for missing-modality robustness. In *Proceedings of the AAAI Conference on Artificial Intelligence*, volume 38, pp. 15483–15491, 2024b.
- Wang, H., Qian, Y., Weng, P., Xia, Z., Dan, W., Xu, Y., and Wang, F. Compass: Complete multimodal fusion via proxy tokens and shared spaces for ubiquitous sensing. *arXiv preprint arXiv:2604.02056*, 2026.
- Wang, T. and Isola, P. Understanding contrastive representation learning through alignment and uniformity on the hypersphere. In *International conference on machine learning*, pp. 9929–9939. PMLR, 2020.
- Wang, W., Tran, D., and Feiszli, M. What makes training multi-modal classification networks hard? In *Proceedings of the IEEE/CVF conference on computer vision and pattern recognition*, pp. 12695–12705, 2020.
- Wei, S., Luo, C., and Luo, Y. Boosting multimodal learning via disentangled gradient learning. In *Proceedings of the IEEE/CVF International Conference on Computer Vision*, pp. 22879–22888, 2025.
- Wei, Y. and Hu, D. Mmpareto: Boosting multimodal learning with innocent unimodal assistance. *arXiv preprint arXiv:2405.17730*, 2024.
- Wei, Y., Li, S., Feng, R., and Hu, D. Diagnosing and re-learning for balanced multimodal learning. In *European Conference on Computer Vision*, pp. 71–86. Springer, 2024.
- Wu, M. and Goodman, N. Multimodal generative models for scalable weakly-supervised learning. *Advances in neural information processing systems*, 31, 2018.
- Yaras, C., Chen, S., Wang, P., and Qu, Q. Explaining and mitigating the modality gap in contrastive multimodal learning. *arXiv preprint arXiv:2412.07909*, 2024.
- Yi, L., Douady, R., and Chen, C. Decipher the modality gap in multimodal contrastive learning: From convergent representations to pairwise alignment. *arXiv preprint arXiv:2510.03268*, 2025.
- Yin, W., Zhou, P., Xiao, Z., Liu, J., Yu, S., Sonke, J.-J., and Gavves, E. Towards uniformity and alignment for multimodal representation learning. *arXiv preprint arXiv:2602.09507*, 2026.
- Yu, T., Kumar, S., Gupta, A., Levine, S., Hausman, K., and Finn, C. Gradient surgery for multi-task learning. *Advances in neural information processing systems*, 33: 5824–5836, 2020.
- Zbontar, J., Jing, L., Misra, I., LeCun, Y., and Deny, S. Barlow twins: Self-supervised learning via redundancy reduction. In *International conference on machine learning*, pp. 12310–12320. PMLR, 2021.
- Zong, D., Ding, C., Li, B., Li, J., and Zheng, K. Balancing multimodal learning via online logit modulation. In *Proceedings of the Thirty-Third International Joint Conference on Artificial Intelligence*, pp. 5753–5761, 2024.

| | |
|--|-----------|
| Appendix | 11 |
| A Theory Proofs | 11 |
| A.1 Proof of Geometric Ambiguity | 11 |
| A.2 Proof of Theorem 3.2 (Uniformity and Effective Rank) | 12 |
| A.3 Proof of Theorem 3.3 (Anchoring Bounds Cross-Modal Drift) | 13 |
| A.4 General dispersive potentials induce repulsive geometry | 14 |
| A.5 Moment-constrained maximum-entropy formulation | 15 |
| B Implementations and Experiment Details | 16 |
| B.1 Datasets Introduction | 16 |
| B.2 Overall Training Procedure and Baseline Implementations | 16 |
| B.3 Training Environment and Computational Overhead | 16 |
| C Geometry Diagnostics and Visualizations | 17 |
| C.1 Unimodal Geometry and Cross-modal Drift Diagnostics | 17 |
| C.2 Cross-modal Similarity Distributions | 18 |
| C.3 Additional Feature Visualizations | 19 |
| D Additional Experiments | 21 |
| D.1 Hyper-parameter Sensitivity | 21 |
| D.2 Robustness to Missing or Corrupted Modalities | 22 |
| D.3 Additional Baselines Compared with Contrastive Learning on CREMA-D | 23 |
| D.4 Plug-in generality for more baselines | 24 |

A. Theory Proofs

Organization. This appendix provides formal proofs for the theoretical claims of DAGR.

A.1. Proof of Geometric Ambiguity

Let $\mathcal{L} = \sum_{m=1}^M \mathcal{L}_{\text{CE}}(W_m z^m, y)$ be the decoupled objective. If $\{z^m\}_{m=1}^M$ is an optimal solution, then there exists a family of orthogonal transformations $\{R_m\}_{m=1}^M$ such that $z'^m = R_m z^m$ is also optimal, provided each R_m preserves linear separability w.r.t. W_m

Proof. Fix a modality m and write $W := W_m \in \mathbb{R}^{K \times d}$, $z := z^m$. The loss $\mathcal{L}_{\text{CE}}(Wz, y)$ depends on z only through the logits $\ell = Wz$. Hence any transformation $z \mapsto z'$ satisfying $Wz' = Wz$ leaves the objective unchanged.

Let $\mathcal{N}(W) = \{v \in \mathbb{R}^d : Wv = 0\}$ be the null space. Choose orthonormal bases $V_0 \in \mathbb{R}^{d \times (d-r)}$ for $\mathcal{N}(W)$ and $V_1 \in \mathbb{R}^{d \times r}$ for $\mathcal{N}(W)^\perp$, where $r = \text{rank}(W)$. Stack $V = [V_1 \ V_0] \in \mathbb{R}^{d \times d}$, which is orthogonal, and note $WV_0 = 0$.

For any orthogonal matrix $Q \in \mathbb{R}^{(d-r) \times (d-r)}$, define

$$R := V_1 V_1^\top + V_0 Q V_0^\top. \quad (15)$$

Step 1: R is orthogonal. Using $V_1^\top V_0 = 0$, $V_1^\top V_1 = I$, $V_0^\top V_0 = I$, and $Q^\top Q = I$,

$$R^\top R = (V_1 V_1^\top + V_0 Q^\top V_0^\top)(V_1 V_1^\top + V_0 Q V_0^\top) \quad (16)$$

$$= V_1 V_1^\top + V_0 Q^\top Q V_0^\top \quad (17)$$

$$= V_1 V_1^\top + V_0 V_0^\top = I. \quad (18)$$

Step 2: R preserves logits, i.e., $WR = W$. Since $WV_0 = 0$,

$$WR = W(V_1 V_1^\top) + W(V_0 Q V_0^\top) \quad (19)$$

$$= W(V_1 V_1^\top) + (WV_0)QV_0^\top \quad (20)$$

$$= W(V_1 V_1^\top). \quad (21)$$

Moreover, every $x \in \mathbb{R}^d$ decomposes as $x = V_1 V_1^\top x + V_0 V_0^\top x$ and $W(V_0 V_0^\top x) = 0$, so $Wx = W(V_1 V_1^\top x)$ for all x , which implies $W = W(V_1 V_1^\top)$. Hence $WR = W$.

Therefore, for any z , we have $W(Rz) = Wz$, and thus $\mathcal{L}_{\text{CE}}(W(Rz), y) = \mathcal{L}_{\text{CE}}(Wz, y)$. Applying the same construction independently to each modality yields $\{R_m\}_{m=1}^M$ with $W_m R_m = W_m$, so $\mathcal{L}(\{R_m z^m\}) = \mathcal{L}(\{z^m\})$. In particular, if $\{z^m\}$ is optimal, then $\{R_m z^m\}$ is also optimal. \square

A.2. Proof of Theorem 3.2 (Uniformity and Effective Rank)

Theorem 3.2 (restated). Let z be a random embedding on the unit sphere ($\|z\|_2 = 1$) with second moment $\Sigma = \mathbb{E}[zz^\top]$. Minimizing the dispersive loss

$$L_d = \log \mathbb{E}[\exp(-t\|z - z'\|_2^2)], \quad z, z' \text{ i.i.d.},$$

is asymptotically equivalent to maximizing Rényi-2 entropy H_2 of the feature distribution. Moreover, uniformity minimization discourages anisotropy / low-rank covariance by reducing $\text{tr}(\Sigma^2)$ and thus increasing the effective rank $\text{Rank}_{\text{eff}}(\Sigma) = (\text{tr} \Sigma)^2 / \text{tr}(\Sigma^2)$.

Proof. Part A: Rényi-2 interpretation (kernel viewpoint). Let p be the feature distribution and define $k_t(z, z') = \exp(-t\|z - z'\|_2^2)$. Then

$$\mathbb{E}_{z, z' \sim p}[k_t(z, z')] = \iint p(z)p(z')k_t(z, z') dz dz'. \quad (22)$$

For a narrow kernel (bandwidth controlled by t), standard KDE arguments give $\mathbb{E}[k_t(z, z')] = C(t, d) \int p(z)^2 dz$ up to a multiplicative constant $C(t, d)$ independent of p . Since $H_2(p) = -\log \int p(z)^2 dz$, minimizing $L_d = \log \mathbb{E}[k_t]$ is equivalent to maximizing $H_2(p)$ up to an additive constant.

Part B: Rewrite on the unit sphere. If $\|z\| = \|z'\| = 1$, then $\|z - z'\|_2^2 = 2 - 2z^\top z'$ and thus

$$k_t(z, z') = \exp(-2t) \exp(2t z^\top z').$$

Part C: Second-order expansion connects to $\text{tr}(\Sigma^2)$. Using $\exp(2tu) = 1 + 2tu + 2t^2 u^2 + O(t^3)$ with $u = z^\top z'$ and taking expectations,

$$\mathbb{E}[k_t(z, z')] = \exp(-2t) \left(1 + 2t \mathbb{E}[z^\top z'] + 2t^2 \mathbb{E}[(z^\top z')^2] + O(t^3) \right).$$

If features are (approximately) centered so that $\mathbb{E}[z] = 0$, then by independence $\mathbb{E}[z^\top z'] = \mathbb{E}[z]^\top \mathbb{E}[z'] = 0$. For the quadratic term, using independence again,

$$\mathbb{E}[(z^\top z')^2] = \mathbb{E}[z^\top (z' z'^\top) z] = \mathbb{E}[z^\top \mathbb{E}[z' z'^\top] z] = \mathbb{E}[z^\top \Sigma z] = \text{tr}(\Sigma \mathbb{E}[zz^\top]) = \text{tr}(\Sigma^2).$$

Therefore, in the centered case,

$$\mathbb{E}[k_t(z, z')] = \exp(-2t) \left(1 + 2t^2 \text{tr}(\Sigma^2) + O(t^3) \right),$$

so minimizing $L_d = \log \mathbb{E}[k_t]$ discourages large $\text{tr}(\Sigma^2) = \|\Sigma\|_F^2$, i.e., discourages anisotropy / low-rank covariance.

Part D: Effective rank. Define $\text{Rank}_{\text{eff}}(\Sigma) := (\text{tr } \Sigma)^2 / \text{tr}(\Sigma^2)$. On the unit sphere, $\text{tr } \Sigma = \mathbb{E} \|z\|_2^2 = 1$, hence

$$\text{Rank}_{\text{eff}}(\Sigma) = \frac{1}{\text{tr}(\Sigma^2)}.$$

Thus reducing $\text{tr}(\Sigma^2)$ increases $\text{Rank}_{\text{eff}}(\Sigma)$, pushing representations away from low-rank collapse. \square

A.3. Proof of Theorem 3.3 (Anchoring Bounds Cross-Modal Drift)

Theorem 3.3 (restated with a tolerance radius). Consider the joint objective

$$\mathcal{L}_{\text{total}} = \mathcal{L} + \lambda_a \mathcal{L}_a + \lambda_d \mathcal{L}_d, \quad (23)$$

where the bounded anchoring term is defined as

$$\mathcal{L}_a := \mathbb{E} \left[(\| \tilde{z}^m - \tilde{z}^n \|_2 - \tau)_+^2 \right], \quad (x)_+ = \max(x, 0), \quad (24)$$

and $\tau \geq 0$ specifies a tolerance radius that preserves modality-specific deviations. Define the non-anchoring part of the objective as

$$\tilde{\mathcal{L}}(\tilde{z}^m, \tilde{z}^n) := \mathcal{L}(\tilde{z}^m, \tilde{z}^n) + \lambda_d \mathcal{L}_d(\tilde{z}^m, \tilde{z}^n). \quad (25)$$

We further define the *irreducible modality gap*

$$\delta := \min_{\tilde{z}} \tilde{\mathcal{L}}(\tilde{z}, \tilde{z}) - \min_{\tilde{z}^m, \tilde{z}^n} \tilde{\mathcal{L}}(\tilde{z}^m, \tilde{z}^n) \geq 0. \quad (26)$$

Let $(\tilde{z}_*^m, \tilde{z}_*^n)$ be a minimizer of $\mathcal{L}_{\text{total}}$. Then the expected *excess* cross-modal drift satisfies

$$\mathbb{E} \left[(\| \tilde{z}_*^m - \tilde{z}_*^n \|_2 - \tau)_+^2 \right] \leq \frac{\delta}{\lambda_a}. \quad (27)$$

Proof. By optimality of $(\tilde{z}_*^m, \tilde{z}_*^n)$, we have

$$\mathcal{L}_{\text{total}}(\tilde{z}_*^m, \tilde{z}_*^n) = \tilde{\mathcal{L}}(\tilde{z}_*^m, \tilde{z}_*^n) + \lambda_a \mathbb{E} \left[(\| \tilde{z}_*^m - \tilde{z}_*^n \|_2 - \tau)_+^2 \right] \quad (28)$$

$$\leq \min_{\tilde{z}} \left\{ \tilde{\mathcal{L}}(\tilde{z}, \tilde{z}) + \lambda_a \mathbb{E} [(\| \tilde{z} - \tilde{z} \|_2 - \tau)_+^2] \right\}. \quad (29)$$

Since $\| \tilde{z} - \tilde{z} \|_2 = 0$ and $\tau \geq 0$, we have $(0 - \tau)_+ = 0$ and thus

$$\min_{\tilde{z}} \left\{ \tilde{\mathcal{L}}(\tilde{z}, \tilde{z}) + \lambda_a \mathbb{E} [(\| \tilde{z} - \tilde{z} \|_2 - \tau)_+^2] \right\} = \min_{\tilde{z}} \tilde{\mathcal{L}}(\tilde{z}, \tilde{z}). \quad (30)$$

On the other hand, by definition of the minimum,

$$\tilde{\mathcal{L}}(\tilde{z}_*^m, \tilde{z}_*^n) \geq \min_{\tilde{z}^m, \tilde{z}^n} \tilde{\mathcal{L}}(\tilde{z}^m, \tilde{z}^n). \quad (31)$$

Combining the inequalities yields

$$\lambda_a \mathbb{E} \left[(\| \tilde{z}_*^m - \tilde{z}_*^n \|_2 - \tau)_+^2 \right] \leq \min_{\tilde{z}} \tilde{\mathcal{L}}(\tilde{z}, \tilde{z}) - \min_{\tilde{z}^m, \tilde{z}^n} \tilde{\mathcal{L}}(\tilde{z}^m, \tilde{z}^n) = \delta, \quad (32)$$

which completes the proof. \square

Corollary (overall drift bound). Although Theorem 3.3 bounds only the drift exceeding the tolerance radius τ , it also implies a bound on the overall cross-modal drift.

Corollary A.1. *Under the conditions of Theorem 3.3,*

$$\mathbb{E} [\| \tilde{z}_*^m - \tilde{z}_*^n \|_2^2] \leq 2\tau^2 + \frac{2\delta}{\lambda_a}. \quad (33)$$

Proof. Let $d = \|\tilde{z}_*^m - \tilde{z}_*^n\|_2$. Since $d \leq \tau + (d - \tau)_+$, we have

$$d^2 \leq (\tau + (d - \tau)_+)^2 \leq 2\tau^2 + 2(d - \tau)_+^2, \quad (34)$$

where the last inequality uses $(a + b)^2 \leq 2a^2 + 2b^2$. Taking expectations and applying Theorem 3.3 yields

$$\mathbb{E}[d^2] \leq 2\tau^2 + 2\mathbb{E}[(d - \tau)_+^2] \leq 2\tau^2 + \frac{2\delta}{\lambda_a} \rightarrow 2\tau^2 (\delta \rightarrow 0), \quad (35)$$

which completes the proof. \square

Interpretation. The quantity δ captures the unavoidable benefit of allowing modality-specific deviations, for instance due to modality-dependent noise or nuisance factors. Consequently, even at the optimum, a non-zero cross-modal drift is permitted, which is consistent with Remark 3.4.

Corollary A.2 (Average pairwise drift for M modalities). *Let*

$$\mathcal{L}_a = \mathbb{E}\left[\frac{1}{M(M-1)} \sum_{m \neq n} \|\tilde{z}^m - \tilde{z}^n\|_2^2\right],$$

and define $\delta := \min_{\tilde{z}} \tilde{L}(\tilde{z}, \dots, \tilde{z}) - \min_{\{\tilde{z}^m\}} \tilde{L}(\{\tilde{z}^m\}) \geq 0$, where \tilde{L} denotes the objective without \mathcal{L}_a and the tied set is $\tilde{z}^1 = \dots = \tilde{z}^M = \tilde{z}$. Let $\{\tilde{z}_*^m\}_{m=1}^M$ minimize $\tilde{L}(\{\tilde{z}^m\}) + \lambda_a \mathcal{L}_a$. Then

$$\mathbb{E}\left[\frac{1}{M(M-1)} \sum_{m \neq n} \|\tilde{z}_*^m - \tilde{z}_*^n\|_2^2\right] \leq \frac{\delta}{\lambda_a} + 2\tau^2.$$

Proof. Identical to Theorem 3.3 by comparing the optimum to the tied family, for which $\mathcal{L}_a = 0$. \square

A.4. General dispersive potentials induce repulsive geometry

The dispersive term used in the main text adopts a uniformity-style RBF form. More generally, however, DAGR can be extended to a broader family of pairwise dispersive potentials. This subsection shows that such objectives share a common geometric property: they induce repulsive updates that push nearby samples apart on the unit hypersphere. This explains why multiple dispersive losses can be reasonable from a geometric perspective, even though the main text focuses on the RBF instantiation for its cleaner entropy-based interpretation.

Lemma A.3 (Repulsive gradients of dispersive potentials). *Let $\{\tilde{z}_i\}_{i=1}^B \subset \mathbb{S}^{d-1}$ be ℓ_2 -normalized embeddings and consider the pairwise dispersive objective*

$$L_d = \frac{1}{B(B-1)} \sum_{i \neq j} \psi(\|\tilde{z}_i - \tilde{z}_j\|_2^2), \quad (36)$$

where $\psi : \mathbb{R}_{\geq 0} \rightarrow \mathbb{R}$ is non-increasing. Then for each i , any valid (sub)gradient satisfies

$$\nabla_{\tilde{z}_i} L_d = \frac{2}{B(B-1)} \sum_{j \neq i} \psi'(\|\tilde{z}_i - \tilde{z}_j\|_2^2) (\tilde{z}_i - \tilde{z}_j), \quad (37)$$

where ψ' denotes the derivative when it exists, or any valid sub-derivative otherwise. Equivalently, the descent direction can be written as

$$-\nabla_{\tilde{z}_i} L_d = \frac{2}{B(B-1)} \sum_{j \neq i} w_{ij} (\tilde{z}_i - \tilde{z}_j), \quad w_{ij} := -\psi'(\|\tilde{z}_i - \tilde{z}_j\|_2^2) \geq 0. \quad (38)$$

Hence, minimizing L_d induces a nonnegative weighted combination of directions pointing away from other samples.

Proof. Fix i and let $d_{ij} := \|\tilde{z}_i - \tilde{z}_j\|_2^2$. Since

$$d_{ij} = (\tilde{z}_i - \tilde{z}_j)^\top (\tilde{z}_i - \tilde{z}_j),$$

its gradient with respect to \tilde{z}_i is

$$\nabla_{\tilde{z}_i} d_{ij} = 2(\tilde{z}_i - \tilde{z}_j).$$

Applying the chain rule to each pairwise term gives

$$\nabla_{\tilde{z}_i} \psi(d_{ij}) = \psi'(d_{ij}) \nabla_{\tilde{z}_i} d_{ij} = 2\psi'(d_{ij})(\tilde{z}_i - \tilde{z}_j).$$

Summing over all $j \neq i$ and multiplying by the prefactor in Eq. (36) yields Eq. (37).

Because ψ is non-increasing, any valid derivative or sub-derivative satisfies $\psi'(u) \leq 0$. Therefore $w_{ij} := -\psi'(d_{ij}) \geq 0$, and the descent direction is a nonnegative weighted sum of vectors of the form $\tilde{z}_i - \tilde{z}_j$, which point away from other samples. \square

Remark. Lemma A.3 shows that repulsive geometry is not unique to the RBF loss used in the main text. Other non-increasing pairwise potentials can also discourage collapse by pushing nearby embeddings apart. However, among these choices, the RBF uniformity objective is especially convenient because it additionally admits the Rényi-2 entropy interpretation used in our theoretical analysis. If optimization is performed directly on the sphere, the corresponding Riemannian gradient is obtained by projecting the Euclidean gradient onto the tangent space, while preserving the same pairwise repulsive structure.

A.5. Moment-constrained maximum-entropy formulation

Beyond the specific instantiation used in the main text, DAGR can be generalized to a broader family of intra-modal dispersive potentials that encourage nearby samples to repel each other on the unit hypersphere. Such losses are geometrically meaningful because they promote representation diversity and discourage collapse. However, the clean entropy-based interpretation used in our theory is specific to the uniformity-style RBF formulation adopted in this work. For this reason, we use the RBF dispersive loss as the default choice in the main text.

Let $\tilde{z}^m = f_m(x^m; \theta)$ denote the ℓ_2 -normalized embedding of modality m , and let Z_θ^m be the corresponding random variable supported on the unit hypersphere. We seek modality-wise representations that are both diverse and geometrically coherent across modalities. A natural idealized formulation is to maximize unimodal entropy while constraining excessive cross-modal drift. For simplicity, we state the constraint for a modality pair (m, n) ; in practice, it can be enforced for each pair or averaged over pairs:

$$\max_{\theta} \sum_{m=1}^M H_2(Z_\theta^m) \quad \text{s.t.} \quad \mathbb{E} \left[(\|\tilde{z}^m - \tilde{z}^n\|_2 - \tau)_+^2 \right] \leq \epsilon, \quad (39)$$

where $H_2(\cdot)$ denotes the Rényi-2 entropy and ϵ specifies a drift budget.

The corresponding Lagrangian is

$$\mathcal{J}(\theta, \lambda_a) = - \sum_{m=1}^M H_2(Z_\theta^m) + \lambda_a \left(\mathbb{E} \left[(\|\tilde{z}^m - \tilde{z}^n\|_2 - \tau)_+^2 \right] - \epsilon \right), \quad \lambda_a \geq 0. \quad (40)$$

Dropping the constant term $-\lambda_a \epsilon$, the objective consists of two parts: (i) maximizing modality-wise Rényi-2 entropy, and (ii) penalizing excess cross-modal drift beyond the tolerance radius τ . By Theorem 3.2, the first term admits a tractable surrogate under the uniformity-style RBF dispersive loss. Specifically, maximizing $H_2(Z_\theta^m)$ can be approximated by minimizing the RBF dispersive objective $\mathcal{L}_d^m(\theta)$ used in Eq. (6). This yields the surrogate objective

$$\min_{\theta} \lambda_d \sum_{m=1}^M \mathcal{L}_d^m(\theta) + \lambda_a \mathbb{E} \left[(\|\tilde{z}^m - \tilde{z}^n\|_2 - \tau)_+^2 \right], \quad (41)$$

which recovers the two components of DAGR: intra-modal dispersion and bounded inter-modal anchoring.

This perspective clarifies why multiple dispersive losses may be geometrically reasonable, while also explaining our preference for the RBF instantiation. More general dispersive potentials can still induce repulsive geometry, but the RBF form is particularly attractive because it provides a direct bridge from dispersion to Rényi-2 entropy and, consequently, to effective-rank control.

B. Implementations and Experiment Details

B.1. Datasets Introduction

CREMA-D (Cao et al., 2014) is an audio–visual dataset designed for speech emotion recognition, which contains 7,442 short video clips of 2–3 seconds performed by 91 actors, annotated with 6 emotion categories. Following prior work, we randomly split the dataset into 6,698 samples for training and 744 samples for testing. This dataset evaluates the model’s ability to learn complementary audio and visual representations under relatively balanced modalities.

Kinetics-Sounds (KS) (Arandjelovic & Zisserman, 2017) is an audio–visual dataset constructed by filtering the Kinetics dataset to retain 34 sound-related action classes that are potentially manifested in both visual and auditory channels. It contains approximately 19k 10-second video clips, with 15k samples for training, 1.9k for validation, and 1.9k for testing. Compared to CREMA-D, KS presents a more challenging setting due to higher intra-class diversity and frequent modality imbalance, making it suitable for evaluating robustness under complex multimodal interactions.

CUB Image-Captions for Clustering (CUBICC) is a bimodal image–text dataset derived from the CUB image caption dataset constructed by Palumbo *et al.* (Palumbo et al., 2024), consisting of bird images paired with corresponding natural language descriptions. The dataset is organized into 8 semantic categories based on bird species, which is adopted to evaluate the model’s ability to disentangle and align multimodal latent spaces under fine-grained semantic supervision, rather than to exhaustively cover all possible modality combinations.

XRF55 (Wang et al., 2024a) is a large-scale multi-RF dataset for indoor human action recognition. It contains 42.9K synchronized samples spanning 55 action classes, collected from 39 subjects over 100 days. Each sample consists of multiple radio-frequency sensing modalities, including Wi-Fi CSI (9 links), RFID phase sequences (23 tags), and mmWave radar measurements, together with synchronized Azure Kinect recordings (RGB, depth, and infrared). Following the official protocol, we use the first 14 trials of each action performed by each subject for training and the remaining 6 trials for testing, resulting in 30.0K training samples and 12.9K test samples. This dataset allows us to evaluate whether DAGR generalizes beyond conventional audio–visual settings to privacy-preserving RF-based multimodal perception with heterogeneous sensing modalities.

B.2. Overall Training Procedure and Baseline Implementations

We incorporate DAGR into the original training objective in a plug-and-play manner, without modifying the backbone architectures or optimization pipeline. Specifically, the overall training loss is defined as

$$\mathcal{L}_{\text{total}} = \mathcal{L} + \mathcal{L}_{\text{DAGR}}, \quad (42)$$

where \mathcal{L} denotes the original task-specific objective (e.g., cross-entropy), and $\mathcal{L}_{\text{DAGR}}$ is applied as an auxiliary regularization term on the intermediate modality embeddings.

Baseline implementation and fairness settings. For all baseline methods, we adopt identical data splits, feature extractors, backbone architectures, batch sizes, optimizers, and learning-rate schedules. Only method-specific components (e.g., gradient modulation, objective reweighting, or fusion strategies) are changed to ensure a fair comparison.

Implementation details of baseline methods. Whenever available, we rely on official implementations or publicly released benchmark codebases. If an official implementation is not available, we re-implement the method following the original paper and match the reported hyper-parameters as closely as possible. For all baselines and their corresponding variants augmented with DAGR, we run experiments with three different random seeds (0, 42, 3407) and report the mean and standard deviation of the results.

B.3. Training Environment and Computational Overhead

All experiments were conducted on a server equipped with a single NVIDIA H100 GPU with 80 GB of VRAM and 128 GB of system memory. Unless otherwise specified, all models were trained and evaluated under identical hardware, software, and optimization settings to ensure fair runtime comparisons.

DAGR is implemented as a lightweight regularization module applied to intermediate modality embeddings and introduces no additional trainable parameters. Its intra-modal dispersion term requires pairwise distance computations within each modality,

Table 6. Training time and computational overhead under different batch sizes on CREMA-D and Kinetics-Sounds. All experiments are conducted on a single NVIDIA H100 GPU.

| Batch Size | CREMA-D | | | Kinetics-Sounds | | |
|------------|--------------|---------------------|-----------|---------------------|---------------------|-----------|
| | Baseline (s) | Baseline + DAGR (s) | Over. (%) | Baseline (s) | Baseline + DAGR (s) | Over. (%) |
| 32 | 22.36 | 25.80 | +15.4 | 89.49 | 102.67 | +14.7 |
| 64 | 21.19 | 23.83 | +12.5 | 86.63 | 95.03 | +9.7 |
| 128 | 21.03 | 23.55 | +12.0 | FAILED ¹ | FAILED ¹ | – |
| 256 | 21.02 | 22.95 | +9.2 | FAILED ¹ | FAILED ¹ | – |

Table 7. Training time and computational overhead under different batch sizes on XRF55 and CUBICC All experiments are conducted on a single NVIDIA H100 GPU.

| Batch Size | XRF55 | | | CUBICC | | |
|------------|--------------|---------------------|-----------|---------------------|---------------------|-----------|
| | Baseline (s) | Baseline + DAGR (s) | Over. (%) | Baseline (s) | Baseline + DAGR (s) | Over. (%) |
| 32 | 258.23 | 272.38 | +5.19 | 68.26 | 78.85 | +15.5 |
| 64 | 255.55 | 257.78 | +0.87 | 64.84 | 71.66 | +10.5 |
| 128 | 247.12 | 248.46 | +0.54 | 71.31 | 76.44 | +7.2 |
| 256 | 246.26 | 244.23 | -0.82 | FAILED ¹ | FAILED ¹ | – |

while the inter-modal anchoring term enforces sample-level alignment across modalities. Both terms are implemented using fully vectorized tensor operations and are activated only during training, incurring no additional cost at inference time.

Table 6 and 7 reports the average per-epoch training time on representative benchmarks, comparing the baseline models with their counterparts augmented by DAGR. Across datasets of different scales and modality compositions, DAGR introduces only a modest increase in training time, remaining well within practical limits on modern GPU hardware.

C. Geometry Diagnostics and Visualizations

C.1. Unimodal Geometry and Cross-modal Drift Diagnostics

Goal and setup. To better understand the geometric effects of DAGR beyond downstream accuracy, we analyze the intermediate representation space using three complementary diagnostics: (i) a *semantic margin* that measures class-wise separability, (ii) an *effective rank* that measures unimodal representation diversity, and (iii) a *cross-modal drift* metric that measures the discrepancy between paired embeddings across modalities. Together, these quantities are designed to track the two failure modes discussed in the main text: intra-modal collapse and sample-level cross-modal drift.

Unless otherwise stated, all quantities are computed from the intermediate modality-wise embeddings used by DAGR after ℓ_2 normalization. We compare the baseline model, a variant with the dispersive term only (**Disp Only**), and the full DAGR model.

Semantic margin Δ_{sem} . To quantify class-wise separability, we define the *semantic margin*

$$\Delta_{\text{sem}} = \mathbb{E}_{y \neq y'} \left[\mathbb{E}_{i \in \mathcal{I}_y, j \in \mathcal{I}_{y'}} \|z_i - z_j\|_2 \right] - \mathbb{E}_y \left[\mathbb{E}_{i, j \in \mathcal{I}_y} \|z_i - z_j\|_2 \right], \quad (43)$$

where \mathcal{I}_y is the index set of samples with class label y , and z denotes the representation used for evaluation.

Geometrically, Δ_{sem} compares *between-class spread* against *within-class compactness*. A larger value means that samples from different classes are farther apart, relative to samples from the same class, and therefore indicates a more semantically organized representation space. This metric is useful because neither dispersion nor anchoring alone directly optimizes class

¹**FAILED:** CUDA OOM in the baseline at this batch size (NVIDIA H100, 80 GB VRAM, AMP enabled). Results at smaller batch sizes confirm DAGR adds <15% overhead on average.

separation: dispersion can increase global spread without necessarily improving semantic organization, while anchoring controls paired cross-modal geometry rather than class structure. Hence, Δ_{sem} serves as an important downstream geometric readout of whether the learned space becomes more semantically discriminative.

Effective rank r_{eff} . To quantify unimodal representation diversity, we track the effective rank of the covariance matrix of unimodal embeddings. Given a covariance matrix Σ with eigenvalues $\{\lambda_i\}_{i=1}^d$, define the normalized spectrum $p_i = \lambda_i / \sum_j \lambda_j$ and the effective rank

$$r_{\text{eff}}(\Sigma) = \exp\left(-\sum_{i=1}^d p_i \log p_i\right). \quad (44)$$

The effective rank measures how broadly variance is distributed across feature directions. If the representation collapses into a narrow low-dimensional subspace, only a few eigenvalues dominate and r_{eff} becomes small. Conversely, a larger effective rank indicates that the representation occupies more directions of the ambient space and is therefore less collapsed. This makes r_{eff} a natural empirical proxy for the role of the dispersive term. It is also consistent with the theoretical discussion in the main text, where the RBF dispersive loss is related to higher Rényi-2 entropy and the avoidance of low-rank solutions.

Cross-modal drift d_{drift} . To quantify sample-level discrepancy across modalities, we measure the average distance between paired cross-modal embeddings:

$$d_{\text{drift}} = \mathbb{E}[\|z_i^m - z_i^n\|_2^2], \quad (45)$$

where (m, n) denotes a modality pair and the expectation is taken over paired samples.

Geometrically, d_{drift} measures how far representations of the *same sample* drift apart across modalities. A large value indicates weak sample-level coherence, meaning that the model has difficulty maintaining consistent cross-modal structure for paired inputs. This directly corresponds to the failure mode targeted by the anchoring term. At the same time, the objective of DAGR is *not* to drive this quantity to zero. Because different modalities may contain modality-specific nuisance factors or information that is not perfectly shared, some non-zero drift is both expected and desirable. Thus, d_{drift} should be interpreted as a bounded-coherence diagnostic rather than a full-alignment target.

How to interpret the three diagnostics together. The three quantities capture different and complementary aspects of multimodal geometry. The semantic margin Δ_{sem} evaluates whether the representation space is organized in a semantically discriminative way. The effective rank r_{eff} evaluates whether unimodal representations remain diverse rather than collapsing into a small subspace. The cross-modal drift d_{drift} evaluates whether paired embeddings across modalities remain geometrically coherent.

Taken together, these diagnostics help disentangle the roles of the two components of DAGR. A dispersive term alone may enlarge the spread of representations and partially affect r_{eff} , but it does not by itself guarantee lower drift or improved semantic organization. Conversely, anchoring alone may reduce excessive cross-modal discrepancy, but without sufficient unimodal diversity the learned space can still be poorly conditioned. The full DAGR objective is designed to improve these quantities jointly: dispersion promotes richer modality-wise geometry, while anchoring limits excessive sample-level drift. For this reason, we use Δ_{sem} , r_{eff} , and d_{drift} as the primary diagnostics throughout our geometric analysis.

C.2. Cross-modal Similarity Distributions

To further analyze how geometry-aware regularization affects cross-modal alignment at the sample level, we examine the distribution of cosine similarities between cross-modal embedding pairs. Specifically, we consider *positive* pairs, where embeddings from different modalities correspond to the same sample, and *negative* pairs formed by randomly mismatched samples. All similarities are computed using ℓ_2 -normalized intermediate embeddings.

Distributional separation metrics. To quantitatively assess the separability between the similarity distributions of positive and negative pairs, we report two complementary metrics that capture different aspects of distributional difference.

First, we measure the mean similarity gap

$$\Delta\mu; =; \mathbb{E}[s_{\text{pos}}] - \mathbb{E}[s_{\text{neg}}], \quad (46)$$

where s_{pos} and s_{neg} denote the cosine similarities of positive and negative pairs, respectively. This metric characterizes the first-order (mean-level) separation between the two distributions. A larger $\Delta\mu$ indicates that, on average, positive pairs are assigned higher similarity scores than negative pairs, reflecting improved global discrimination.

However, mean separation alone does not fully describe how well the two distributions are distinguished. Two distributions may have similar means yet differ substantially in dispersion, overlap, or tail behavior. To capture such effects, we additionally report the Kolmogorov–Smirnov (KS) distance D_{KS} between the empirical distributions of s_{pos} and s_{neg} . The KS distance is defined as the maximum absolute difference between their cumulative distribution functions,

$$D_{\text{KS}} = \sup_x |F_{\text{pos}}(x) - F_{\text{neg}}(x)|, \quad (47)$$

where F_{pos} and F_{neg} denote the empirical CDFs of positive and negative similarities, respectively.

Unlike $\Delta\mu$, which summarizes only the average separation, D_{KS} measures the largest distributional discrepancy at any similarity threshold. It is sensitive to higher-order characteristics such as variance, skewness, and tail overlap, and therefore provides a more holistic view of how well the two similarity distributions are separated across their entire support. Together, $\Delta\mu$ and D_{KS} offer complementary perspectives on distributional separability, capturing both mean-level and shape-level differences.

Observed effects of geometry-aware regularization. As shown in Fig. 4(a), the baseline exhibits highly overlapping similarity distributions for positive and negative pairs, indicating weak cross-modal discriminability. This is reflected by a near-zero mean gap ($\Delta\mu = +0.00061$) and a small KS distance ($D_{\text{KS}} = 0.02577$), suggesting that matched pairs are not consistently ranked above mismatched ones.

After incorporating dispersion together with alignment/anchoring (Fig. 4(b)), the positive and negative distributions become substantially more separated. Both the mean gap ($\Delta\mu = +0.01415$) and the KS distance ($D_{\text{KS}} = 0.09267$) increase markedly, indicating improved cross-modal discriminability. This behavior is consistent with the intended effect of the regularizer: dispersion prevents representation collapse, while anchoring reduces sample-level cross-modal drift, jointly reshaping the similarity geometry.

Implications for retrieval. Finally, Fig. 4(c) reports retrieval-style performance measured by Recall@K, which evaluates the probability that a true cross-modal match appears among the top- K retrieved candidates. Consistent with the improved distributional separation, the regularized model achieves higher Recall@K across a wide range of K , with especially pronounced gains for larger K . This suggests that the learned similarity geometry not only improves average separability, but also yields more favorable global ranking behavior for cross-modal retrieval.

C.3. Additional Feature Visualizations

To qualitatively examine the effect of geometry-aware regularization on multimodal representation structure, we provide additional 2D visualizations on three datasets: CREMA-D, CUB Image-Captions for Clustering (CUBICC), and XRF55. For each dataset, we project intermediate multimodal embeddings into two dimensions using t-SNE (or PCA when specified), where each point corresponds to a single sample and colors denote semantic categories. For paired modalities (e.g., audio–visual or image–caption), samples from the same instance share the same label, allowing us to inspect cross-modal consistency.

CREMA-D. Figure 5 visualizes multimodal embeddings on CREMA-D. The baseline exhibits noticeable overlap between emotion categories and fragmented cluster structure, with limited alignment between paired modalities. In contrast, incorporating geometry-aware regularization leads to more compact class-wise clusters and improved co-localization of audio and visual embeddings within each emotion category, indicating enhanced intra-modal structure and more stable cross-modal consistency.

CUBICC. Figure 6 shows the visualization results on the CUBICC dataset. While the baseline already exhibits partial semantic separation, image and caption embeddings of the same category often form loosely overlapping or fragmented structures. With geometry-aware regularization, clusters become more coherent and better separated, and paired image–caption embeddings display improved overlap within each semantic category, suggesting enhanced semantic organization without enforcing rigid global alignment.

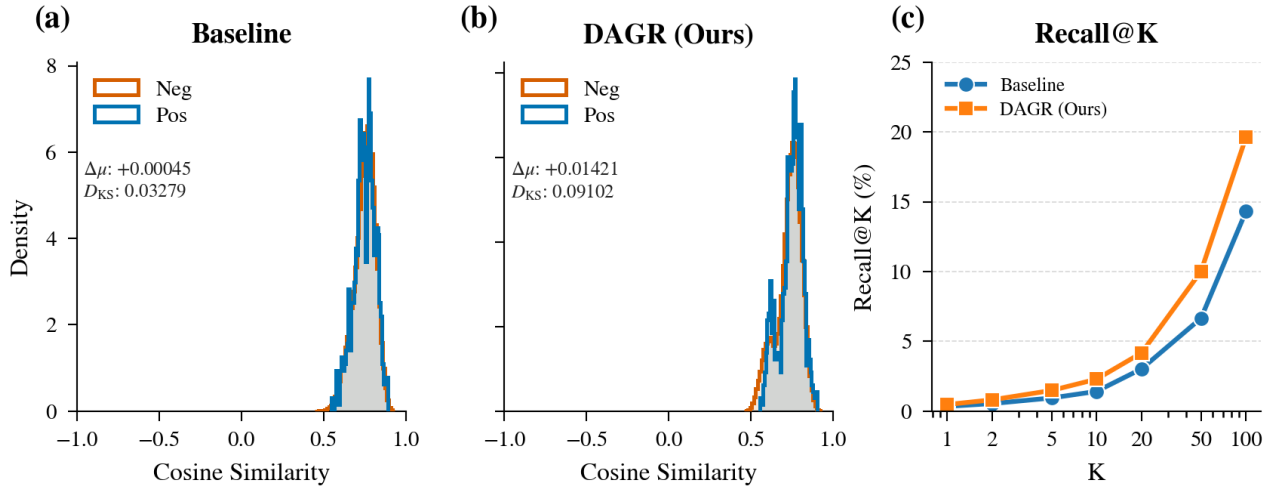


Figure 4. **Cross-modal similarity geometry.** (a) Cosine similarity distributions between positive (matched) and negative (mismatched) cross-modal pairs under the DGL baseline. (b) The corresponding distributions after adding a dispersive loss with an alignment/anchoring component, showing increased separation (larger $\Delta\mu$ and D_{KS}). (c) Retrieval performance measured by Recall@K, where improved separability translates into higher recall.

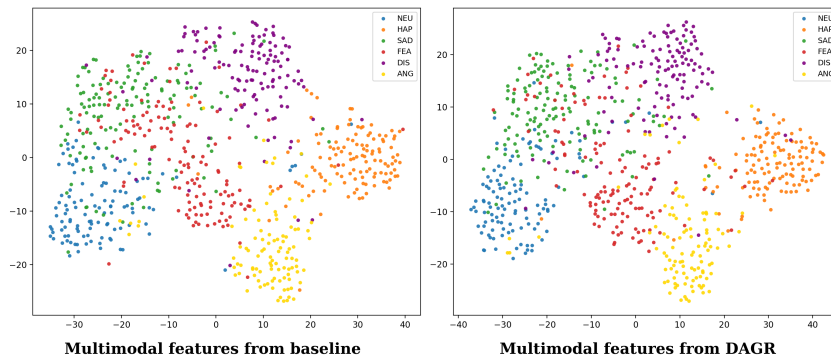


Figure 5. t-SNE visualization of multimodal embeddings on CREMA-D. DAGR produces more compact and better-aligned semantic clusters compared with the baseline.

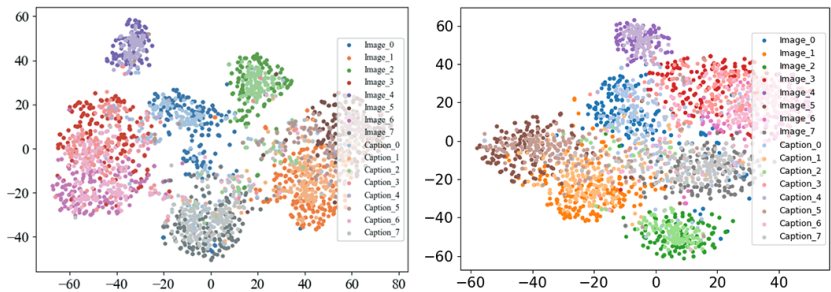


Figure 6. t-SNE visualization of multimodal embeddings on CUBICC. DAGR improves semantic compactness and stabilizes image-caption alignment relative to the baseline.

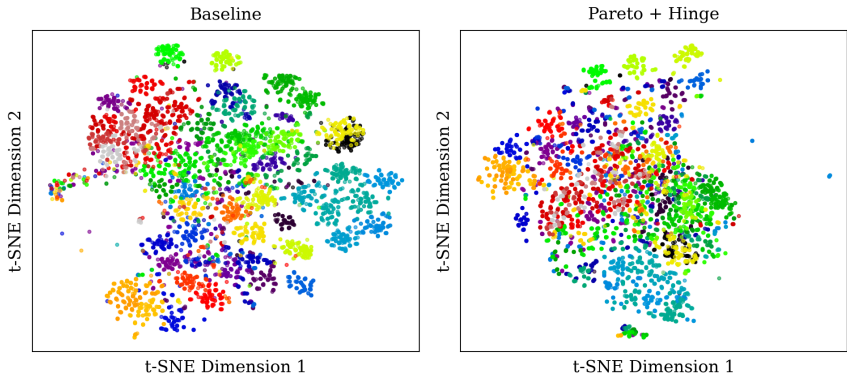


Figure 7. t-SNE/PCA visualization of multimodal embeddings on X-Fi. DAGR yields clearer cluster separation and more consistent cross-modal structure.

XRF55. Figure 7 presents the visualization on the XRF55 dataset. The baseline representations show substantial inter-class mixing and inconsistent cross-modal alignment. After applying geometry-aware regularization, semantic clusters become more distinguishable, and paired modalities exhibit clearer co-localization, reflecting improved representation geometry under higher noise and heterogeneity.

We emphasize that these visualizations are intended for qualitative inspection only and do not fully capture the high-dimensional geometry. Nevertheless, the observed trends are consistent across datasets and align with the quantitative improvements reported in clustering performance and geometric diagnostics (Appendix C.1).

D. Additional Experiments

D.1. Hyper-parameter Sensitivity

Our method introduces two weighting coefficients, λ_d and λ_{inter} , to balance intra-modal compactness and inter-modal alignment. In principle, tuning these two hyper-parameters also depends on the hinge loss threshold τ , since the effective contribution of the hinge term is jointly determined by both the margin τ and the loss weights. As a result, naively performing a grid search over $(\lambda_d, \lambda_{inter}, \tau)$ would lead to a large and unstable hyper-parameter space.

Sensitivity to λ_d and λ_{inter} . To first isolate the effect of the two weighting coefficients, we fix the hinge threshold to $\tau = 0$ and conduct a two-dimensional grid search over $(\lambda_d, \lambda_{inter})$. Figure 8 shows the resulting performance heatmaps on CREMA-D and Kinetics-Sound.

From the results, we observe that moderate values of both λ_d and λ_{inter} generally lead to better performance, while overly large weights do not consistently improve accuracy. This suggests that excessively emphasizing the auxiliary contrastive objectives may dominate the optimization process and suppress task-relevant discriminative cues learned by the primary classification loss. Moreover, strong intra-/inter-regularization may over-constrain the feature geometry, reducing representation flexibility and harming generalization.

Joint sensitivity of β and τ . Motivated by the above observations, we further adopt a Pareto-style parameterization that controls the total regularization strength using a single scalar $\beta = \lambda_d + \lambda_{inter}$, while maintaining a balanced trade-off between intra-modal compactness and inter-modal alignment. Specifically, we consider $\beta \in \{0.1, 0.15, 0.2\}$, which significantly reduces the hyper-parameter search space and improves training stability.

We then conduct an ablation study on the hinge threshold $\tau \in \{0, 0.25, 0.5\}$ under different values of β . Figure 9 visualizes the joint sensitivity of β and τ on CREMA-D and Kinetics-Sound. Overall, the results indicate that our method is relatively robust to moderate variations of τ , while excessively large margins may degrade performance when combined with strong regularization. This further supports our choice of using a small β together with a mild hinge threshold.

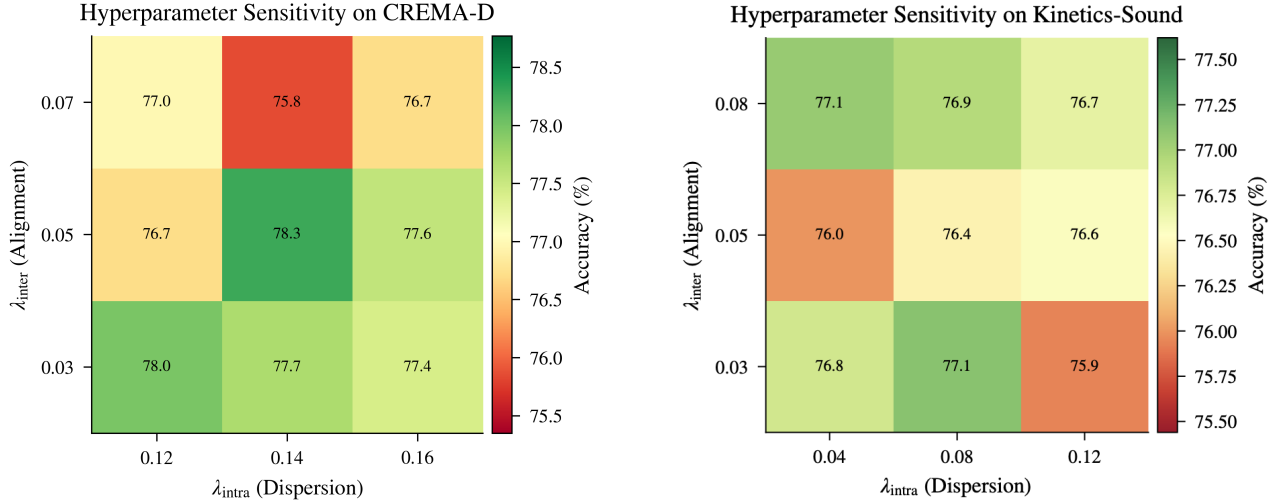


Figure 8. Sensitivity analysis of λ_d and λ_{inter} with the hinge threshold fixed to $\tau = 0$. Left: CREMA-D. Right: Kinetics-Sound.

D.2. Robustness to Missing or Corrupted Modalities

We further evaluate DAGR under *test-time modality degradation* to directly validate the motivation in Sec. 1: when one modality becomes partially missing or corrupted, a robust multimodal model should degrade *gracefully*. Unless otherwise specified, we corrupt *only one* modality at a time during inference while keeping all other modalities unchanged.

CREMA-D: missing and corruption stress tests. For the audio-visual setting on CREMA-D, we consider both *missingness* and *sensor-like corruptions*. (i) **Random missingness.** With probability $p \in [0, 1]$, we replace a modality with a missing placeholder at test time (feature-level masking), resulting in missing-audio and missing-visual curves. (ii) **Audio noise.** We inject additive noise with different SNR levels (dB) to simulate degraded audio acquisition. (iii) **SpecAugment / frame-drop / cutout.** We apply standard modality-specific corruptions: SpecAugment masks a fraction of time/frequency bins on audio features, frame-drop randomly removes a fraction of frames from the visual stream, and cutout occludes a random rectangular region with a given area ratio.

X-FI: dropout corruption. We first evaluate robustness to *partial feature loss* by progressively applying random dropout to a single modality at test time, while keeping all other modalities unchanged. Specifically, for the selected modality we randomly mask a fraction ρ of its feature dimensions or tokens (drop ratio $\rho \in [0, 1]$) before inference. This setting simulates scenarios where a modality is only partially available due to occlusion, packet loss, or unstable sensing.

X-FI: Gaussian corruption. Next, we study robustness to *additive sensor noise* by injecting Gaussian noise into one modality at test time. For modality m , the corrupted input is constructed as $\tilde{\mathbf{x}}^{(m)} = \mathbf{x}^{(m)} + \sigma \cdot s^{(m)} \epsilon$, where $\epsilon \sim \mathcal{N}(0, 1)$, σ controls the noise strength, and $s^{(m)}$ is a modality-specific scale to normalize noise magnitude across modalities. We sweep σ from weak to strong corruption and report the resulting degradation curves.

X-FI: random missingness. Finally, we evaluate robustness to *temporal or segment-level modality absence* by randomly masking parts of a modality. Concretely, for the selected modality, each temporal step or segment is independently removed with probability p (drop rate $p \in [0, 1]$), while all other modalities remain intact. This setting simulates intermittent sensor failures or missing data streams, which are common in real-world deployments.

Discussion. Fig. 10 and Figs. 11–13 provide a direct robustness diagnosis beyond standard unimodal ablations. Across datasets, performance degrades monotonically as corruption severity increases, validating these perturbations as meaningful stress tests. Overall, DAGR tends to achieve higher accuracy and smoother degradation trends when a single modality becomes unreliable, indicating improved robustness of multimodal fusion.

On X-FI, the gains are particularly pronounced for mmWave and WiFi under moderate-to-severe corruption, where the

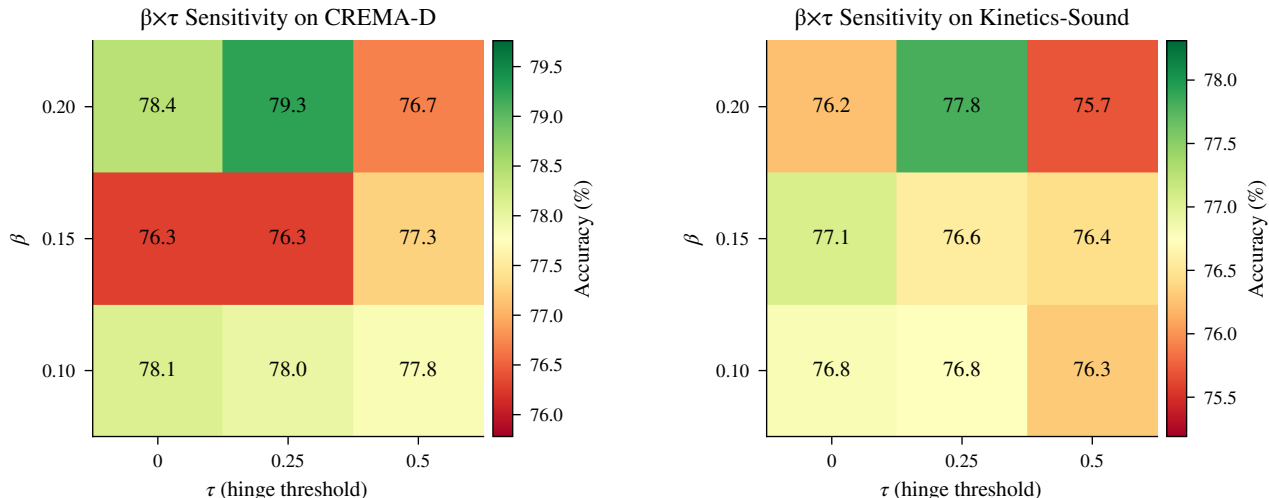


Figure 9. Joint sensitivity analysis of total regularization strength β and hinge threshold τ across two datasets. Left: CREMA-D. Right: Kinetics-Sound.

baseline suffers sharper drops. For RFID, partially corrupted inputs can be more harmful than fully missing ones, suggesting that misleading low-quality signals may interfere with fusion; in these regimes, DAGR maintains a clearer advantage, consistent with stronger resistance to unreliable modality information. On CREMA-D, DAGR improves robustness in the low-to-moderate degradation regime across multiple corruption types and remains competitive under severe corruption, supporting the claim that DAGR alleviates geometric pathologies that otherwise amplify sensitivity to modality degradation.

D.3. Additional Baselines Compared with Contrastive Learning on CREMA-D

Setup. We report results on CREMA-D with four additional controls designed to disentangle the effects of (i) always-on cross-modal coupling (naive alignment), (ii) redundancy-reduction objectives commonly used in non-contrastive/self-supervised learning (VICReg-/Barlow-style), and (iii) feature normalization alone (unit-sphere projection). All methods use the same backbone, optimization schedule, and evaluation protocol as in the main experiments; only the specified regularization term or normalization operation is changed.

Results and Discussion. As shown in Table 8, **naive alignment** and **VICReg-style** regularization achieve competitive multimodal accuracy (77.98 and 78.12), but their improvements do not translate into consistently stronger unimodal performance: VICReg-style notably underperforms on audio (59.18), and naive alignment, while boosting the visual branch (72.21), yields a smaller gain on audio (60.65). In contrast, **our method** attains the best multimodal accuracy (78.16) and the best audio accuracy (62.98), while remaining competitive on visual (72.10). This pattern supports our motivation that *always-on invariance/coupling* can over-constrain modality-specific features, whereas our bounded anchoring combined with dispersive regularization better preserves modality-unique information while still improving cross-modal fusion. Finally, the **unit-sphere only** control provides limited gains (75.81 multimodal), suggesting that the improvement is not explained by normalization alone but requires explicit geometric regularization.

Why our regularization is not contrastive learning. It is important to distinguish our objective from contrastive (InfoNCE-style) learning and invariance-driven paired objectives. Contrastive learning performs *instance discrimination* by comparing each positive pair against a set of negatives, e.g.,

$$\mathcal{L}_{\text{InfoNCE}} = -\mathbb{E}_i \log \frac{\exp(\text{sim}(\mathbf{z}_i^{(a)}, \mathbf{z}_i^{(v)})/t)}{\sum_j \exp(\text{sim}(\mathbf{z}_i^{(a)}, \mathbf{z}_j^{(v)})/t)}, \quad (48)$$

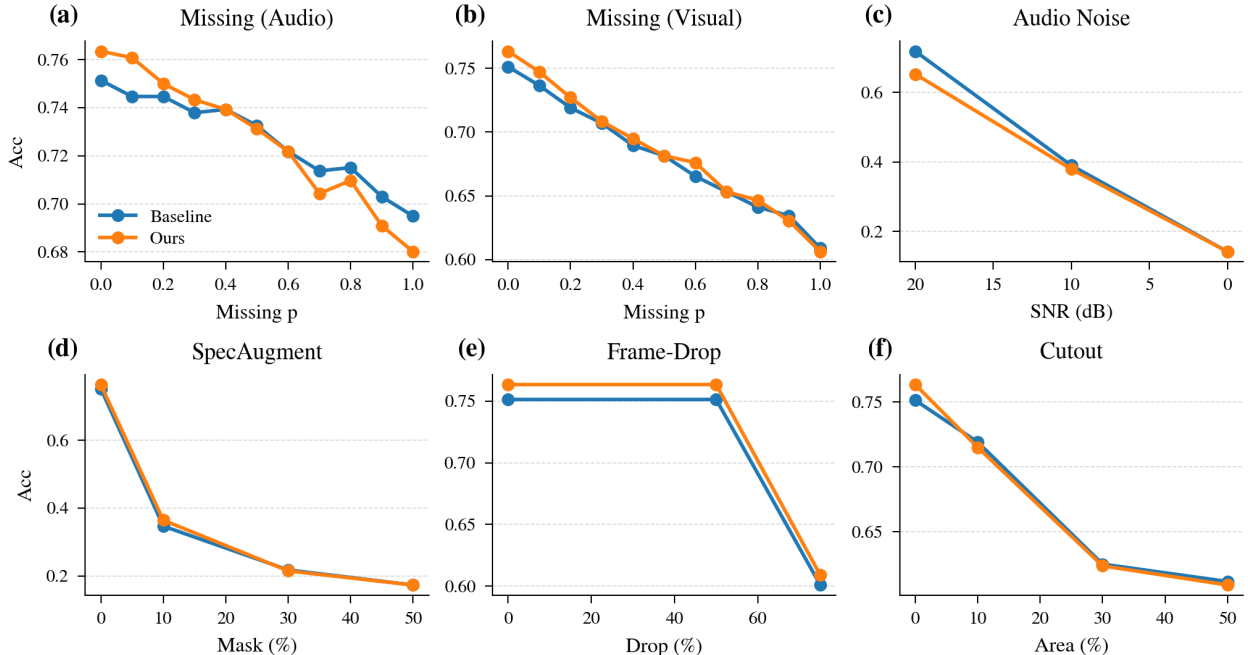


Figure 10. **Robustness under missing or corrupted modalities on CREMA-D.** We evaluate test-time degradation by (a) missing audio, (b) missing visual, (c) additive audio noise (SNR sweep), and modality-specific corruptions including (d) SpecAugment, (e) frame-drop, and (f) cutout. DAGR generally exhibits improved robustness in the low-to-moderate degradation regime and maintains competitive performance under severe corruption, yielding smoother degradation trends than the baseline.

which *always* increases the positive similarity while *repelling* all other instances. In contrast, our anchoring term is *bounded* and does not enforce global invariance:

$$\mathcal{L}_{\text{anchor}} = \mathbb{E}_i \left[\left(\left\| \tilde{\mathbf{z}}_i^{(a)} - \tilde{\mathbf{z}}_i^{(v)} \right\|_2 - \tau \right)_+^2 \right]. \quad (49)$$

Its gradient is *exactly zero* whenever $\|\tilde{\mathbf{z}}_i^{(a)} - \tilde{\mathbf{z}}_i^{(v)}\|_2 \leq \tau$, meaning we do not keep pulling paired embeddings together once they are within an acceptable deviation band. Therefore, our method is not a contrastive objective (no negatives, no softmax normalization), and it is not a pure invariance constraint either.

D.4. Plug-in generality for more baselines

In addition to testing different baselines in CREMA-D (shown in Fig 3), we test the plug-in generality of DAGR in a heterogeneous RF sensing setup on XRF55. Following the X-Fi benchmark protocol, we compare the baseline against the baseline + DAGR configuration. As shown in Table 9, the combined configuration improves all seven observed-modality scenarios and raises the 7-scenario average from 79.55% to 83.44% (+3.89). The gains are especially pronounced in low-modality settings such as Only WiFi, Only RFID, and WiFi+RFID, suggesting that geometry-aware regularization is particularly helpful when cross-modal completion is more challenging.

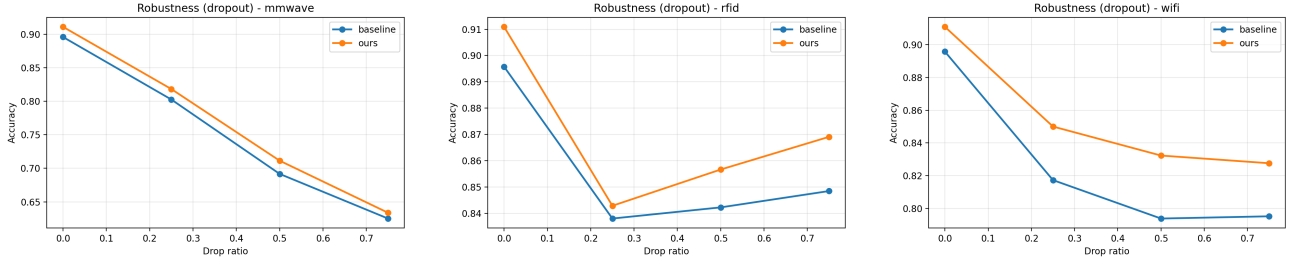


Figure 11. **Robustness under dropout on X-FI.** We progressively drop a fraction ρ of features from one modality at test time, while keeping the other modalities intact. From left to right: mmWave, RFID, and WiFi. DAGR attains higher accuracy and degrades more gracefully than the baseline, especially under moderate-to-severe dropout.

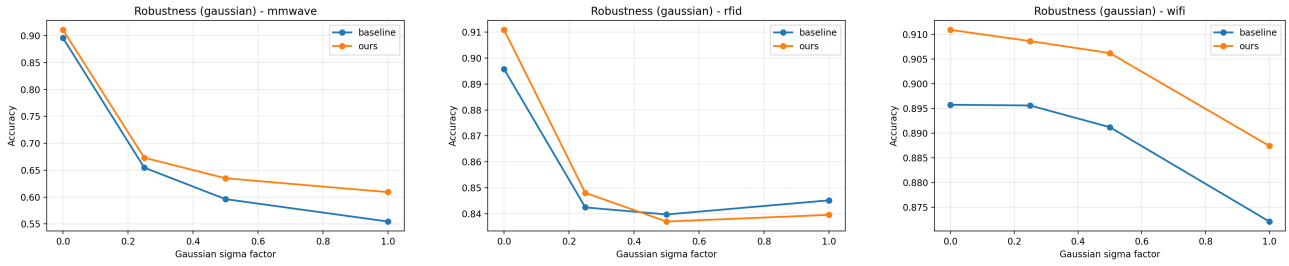


Figure 12. **Robustness under Gaussian noise on X-FI.** We inject additive Gaussian noise with factor σ into a single modality at test time. From left to right: mmWave, RFID, and WiFi. DAGR shows improved robustness under noisy inputs (notably for mmWave and WiFi) and generally degrades more smoothly than the baseline as noise increases.



Figure 13. **Robustness under random missingness on X-FI.** We randomly mask temporal steps or segments of one modality with probability p at test time. From left to right: mmWave, RFID, and WiFi. DAGR maintains higher accuracy and better stability under increasing modality missingness.

Table 8. CREMA-D results with additional controls compared with contrastive/invariance-driven objectives. “Naive Align” enforces always-on per-sample cross-modal coupling. “Unit-sphere only” isolates the effect of normalization without any additional regularization losses.

| Method | CREMA-D | | |
|----------------------------|------------|------------|------------|
| | Audio | Visual | Multi |
| Naive Align (always-on) | 60.65±0.86 | 72.21±1.07 | 77.98±1.11 |
| VICReg-style (inv+var+cov) | 59.18±1.67 | 71.35±1.00 | 78.12±0.94 |
| Barlow Twins-style (decor) | 59.09±0.62 | 61.32±3.41 | 71.07±0.81 |
| Unit-sphere only | 60.65±1.30 | 69.84±0.22 | 75.81±1.52 |
| Ours | 62.98±0.50 | 72.10±0.55 | 78.16±0.38 |

Table 9. Accuracy (%) on the XRF55 dataset under the X-Fi benchmark protocol. **Baseline** denotes the base reconstruction-only configuration, and DAGR augments it with geometry-aware regularization. **Imp** \uparrow reports the absolute improvement of DAGR over **Baseline**.

| Scenario | Baseline | Baseline + DAGR | Imp \uparrow |
|-------------|----------|-----------------|----------------|
| Only mmWave | 88.55 | 90.56 | +2.01 |
| Only WiFi | 77.27 | 83.59 | +6.32 |
| Only RFID | 44.23 | 49.18 | +4.95 |
| mmWave+WiFi | 91.86 | 94.38 | +2.52 |
| mmWave+RFID | 89.91 | 90.58 | +0.67 |
| WiFi+RFID | 74.55 | 80.82 | +6.27 |
| All | 90.45 | 95.00 | +4.55 |
| 7-Avg | 79.55 | 83.44 | +3.89 |